TECHNISCHE UNIVERSITÄT WIEN
Vienna University of Technology

ILSB INSTITUTE OF LIGHTWEIGHT DESIGN AND STRUCTURAL BIOMECHANICS

DIPLOMARBEIT

Simulation of Crack Formation in Thin Copper Films on Polyimide Substrate

ausgeführt zum Zwecke der Erlangung
des akademischen Grades eines Diplom-Ingenieurs
unter der Leitung von

O.Univ.Prof. Dipl.-Ing. Dr.techn. Franz RAMMERSTORFER
Dipl.-Ing. Florian TOTH

Institut für Leichtbau und Struktur-Biomechanik (E317)

eingereicht an der Technischen Universität Wien
Fakultät für Maschinenwesen und Betriebswissenschaften

von

Andreas WIESINGER, BSc.
0826121
Niedersulzerstrasse 29
2225 Loidesthal

Wien, am 10. April 2014 Andreas Wiesinger

Danksagung

Zwischen Juli 2013 und März 2014 habe ich an dieser Diplomarbeit gearbeitet. Dabei erhielt ich viel Hilfe und Unterstützung und dafür möchte ich mich an dieser Stelle bedanken.

Zu Beginn danke ich meinen Betreuern Professor Franz Rammerstorfer und DI Florian Toth für die hervorragende Betreuung und für diese sehr lehrreiche Zeit. In zahlreichen Gesprächen habe ich viele neue Erfahrungen sammeln können.

Aufgrund der Finanzierung dieses Projekts durch den FWF war ich im angegebenen Zeitraum am Institut für Leichtbau und Struktur- Biomechanik angestellt. Ich möchte mich bei allen Mitarbeitern für diese sehr schöne und lehrreiche Zeit und für den Einblick in das wissenschaftliche Arbeiten bedanken.

Auch den Projektpartnern J. Megan Cordill, Professor Gerhard Dehm und Mag. Vera Marx möchte ich für die freundliche Zusammenarbeit danken.

Natürlich danke ich auch meiner Familie, allen voran meinen Eltern, für jegliche Art von Unterstützung. Ohne diese wäre ein Studium, in der Form wie ich es erleben durfte, nicht möglich gewesen. Meiner Tante Roswitha danke ich für das Korrekturlesen dieser Arbeit.

Zum Schluss danke ich noch meiner Freundin Katharina für ihr Verständnis in Zeiten, die ich eher meinem Studium gewidmet habe.

Zusammenfassung

Simulation der Rissbildung in dünnen Kupferfilmen auf Polyimid–Substrat

Diese Arbeit behandelt die nichtlineare Finite Elemente Analyse eines flexiblen Filmsystems. Solche Schichtverbunde sind derzeitig Gegenstand von Forschungsarbeiten im Bereich der Materialwissenschaften. Auch diese Arbeit ist Teil einer Forschungsarbeit in Zusammenarbeit mit dem Max–Plank–Institut für Eisenforschung (MPIE) und dem Erich–Schmid–Institut für Materialwissenschaften der Österreichischen Akademie der Wissenschaften im Rahmen eines FWF–Projekts (Projektleitung: J. Megan Cordill).

Diese flexiblen Filmsysteme werden im praktischen Einsatz hohen Dehnungen ausgesetzt, bei denen Risse in den Metallfilmen entstehen können.

Der Schichtverbund besteht aus einem Kupferfilm auf Polyimidsubstrat. Zwischen diesen beiden Schichten befindet sich ein sehr dünner Chromfilm, welcher die Verbindung der zuvor genannten Schichten verbessern soll. Mit streifenförmigen Proben solcher Schichtsysteme wurden Zugversuche am MPIE durchgeführt. Ergebnisse aus diesen Experimenten werden in der vorliegenden Arbeit mit Ergebnissen aus numerischen Simulationen verglichen.

Es wurden 2D FE–Modelle im verallgemeinerten ebenen Verzerrungszustand erstellt. Die Modellierung der Rissbildung in den Metallfilmen erfolgt durch die Integration von Kohäsivzonenelementen in das FE–Netz. Mit diesen Kohäsivzonenelementen werden jedoch nicht gezielte Fehlstellen in das System eingebracht, an denen dann die Filmrisse entstehen. Stattdessen wird eine Vielzahl dieser Kohäsivzonen in das Modell eingefügt, und deren Parameter werden statistisch verteilt, um eine möglichst realitätsnahe Evolution der räumlichen Verteilung der Risse in den Metallfilmen zu modellieren. Es wurden drei verschiedene Modelle erstellt, welche sich durch die Kupferschichtdicke unterscheiden. Es wurden Analysen mit 50, 100 und 200 nm dicken Kupferschichten durchgeführt. Versuche haben deutlich gezeigt, dass aufgrund von unterschiedlichen Gefügeeigenschaften und Verfestigungsmechanismen eine Abhängigkeit der Materialparameter von der Schichtdicke

besteht. Da die Materialparameter sehr schwer zu messen und auch wenige Studien zu finden sind, war eine große Anzahl an Parameterstudien mit der Variation der Materialparameter in den Metallfilmen unvermeidlich. Mit Hilfe dieser Parameterstudien konnten die zuvor durchgeführten Experimente durch die FE–Simulationen relativ gut reproduziert werden. Um einen Vergleich der FE–Analysen mit den Experimenten vom MPIE herstellen zu können, wurden Programme für die Datenauswertung erstellt. Mit diesen Auswertewerkzeugen werden Vergleichsparameter wie Rissdichten, gemittelte Spannungen und Rissbreiten automatisch nach der Simulation berechnet. Mit den Parameterstudien und dem an das Problem angepassten Postprocessing konnten die Auswirkungen von Materialparametern auf das Modell sehr gut erfasst und einige Besonderheiten dieser flexiblen Filmsysteme erklärt werden.

Abstract

This thesis deals with the non–linear finite elemente analysis of flexible film systems. Currently these film systems are an important research issue in material science. The thesis is part of a research work in cooperation with the Max–Plank–Institut für Eisenforschung (MPIE) Düsseldorf and the Erich–Schmid–Institut of the Austrian Academy of Sciences, Leoben.

Flexible film systems suffer in practical applications on high global elongations. These elongations may lead to the formation of cracks in the metal films. The simulation of such crack formations is also part of the FE-analyses presented here. Flexible film systems are like laminates. The here considered laminate is made of a copper film on polyimide substrate. In order to improve the bonding between copper and the substrate a very thin chrome layer is integrated between these layers. Experiments were made with such samples by the MPIE, and their results are used to be compared with the results from FE–analyses.

For the FE–analyses a two dimensional FE–model with generalized plain strain ele-

ments was created. To enable the simulation of the evolution of the formation of cracks in the metal films a high number of cohesive zone elements were integrated in the FE–mesh. The initiation parameters of the cohesive zone elements are statistically distributed to allow a more realistic spatial distribution of the occurred cracks in the metal films. Three different FE–models were created which differentiate in the copper layer thickness. Considerations with 50, 100 and 200 nm copper layers were made. These models differentiate not only in the thickness of the copper layer. The film thickness has a high influence on the morphology and hardening mechanisms and these effects have high influences on material parameters. Experiments have clearly shown this behaviour. Since material parameters of thin films are hard to determine, parameter studies with variation of the material parameters in the metal films are required in order to find proper parameters by comparison with experimental results. Some results of the parameter studies coincide well with the before made experiments. The comparison of FE–analysis with the experiments is not convenient with available postprocessing tools. So creating convenient postprocessing tools is also a challenge of this thesis. The developed tools provide an automatic computation of mean stresses, crack densities and crack widths after the simulation. The parameter studies showed the influences of the different material parameters quite well. Thus, some behaviours of these flexible film systems could be explained.

Contents

Chapter 1

Introduction

1.1 Copper films on polyimide substrate

Metal Films on polymer substrates in flexible electronics like flexible displays, printed memory, smart textiles, flexible batteries, photovoltaics and much more became an important area in material science [4, 7]. For the use and production of flexible electronic devices and sensors it's important to investigate the mechanical and electrical properties of metal films on polymer substrates. The size of these devices ranges from a few square centimetres to large wearable smart textiles. The requirements for flexible electronics are very high. Stretching and compressing must not lead to mechanical or electrical failing. The thickness of these metal films ranges from a few nanometres to micrometres. The material parameters of such thin metal films are not comparable with those of bulk materials and the determination is a problem. Commonly used substrates are polyesters, polyethyleneterephthate (PET), polyethylenenaphthate (PEN), polycarbonate (PC), polyimide (PI), polyetherimide (PEI) and polyvinyl fluoride (PVF). The thickness of the substrates normally ranges between 50 µm and 200 µm.

It is important to measure the behaviour of the film and the substrate together because there is a high influence of the substrate on the laminate properties [4, 6]. A free standing ductile metal film during tensile straining forms a neck that leads to failure (Fig. 1.1a). But a ductile metal film on polymer substrate is able to suffer a lot more stretching. The substrate suppresses the strain localization that leads to failure (Fig. 1.1b). But this effect

depends on the bonding quality of the laminate. In case of delamination the film stands free and strain localisation is not suppressed. Brittle metal films like Cr, W, Ti or Ta will

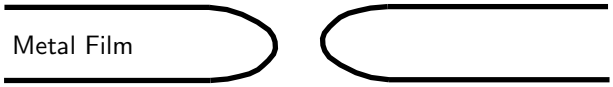

(a) Ductile metal film under tensile loading.

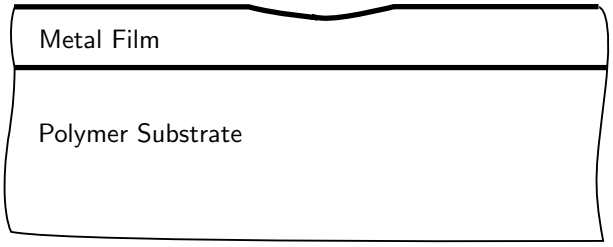

(b) Ductile metal film on polyimide substrate under tensile loading

Figure 1.1: Influence of polymer substrates on metal films

fracture almost immediately under tensile loading. The polymer substrate is not able to prevent failure like at ductile metal films.

As mentioned before the adhesion of metal–polymer interface is important to improve the stretchability of flexible film systems. The addition of an interlayer film between the film and substrate is a common route to improve the adhesion. Therefore, brittle Cr, W, Ti or Ta films with a thickness of 10 – 30 nm are used.

Here are examined just copper films on polyimide substrate under tensile loading. These two layers are separated by a thin chrome layer with 10 nm thickness in order to improve adhesion strength between copper film and polyimide substrate. Figure 1.2 shows the assembly of the three layers. The considerations include three different copper layers with the thicknesses 50, 100 and 200 nm in order to examine their influence. The layer thickness has also an influence on the material properties due to different grain sizes and hardening mechanisms [4, 8]. The polyimide layer has a thickness of 50 µm.

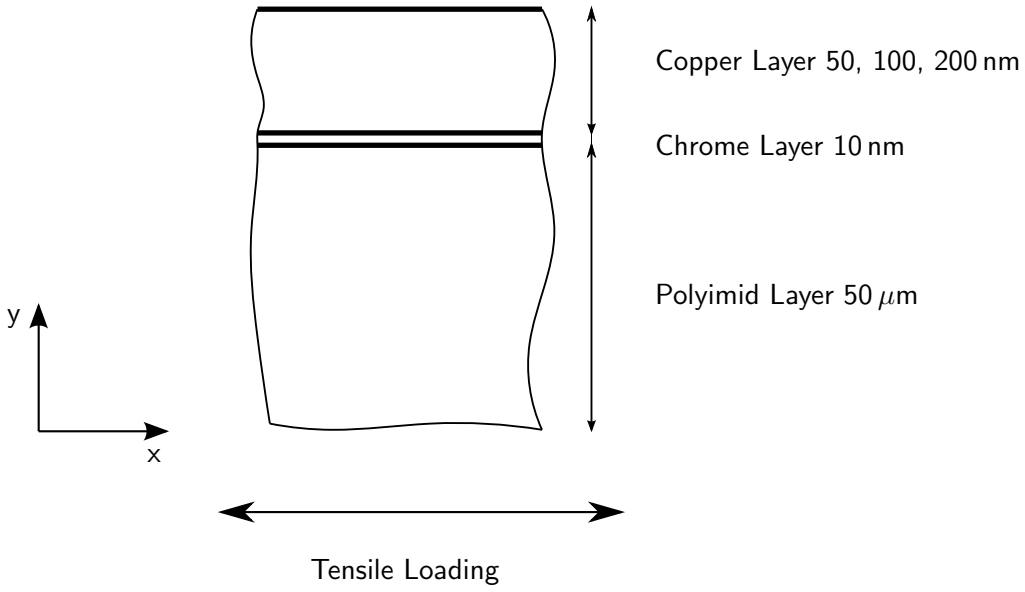

Figure 1.2: Assembly of the flexible film system.

1.2 Experiments and measurements

The Max–Plank–Institute für Eisenforschung (MPIE) and the Erich–Schmid–Insitut of the Austrian Academy of Sciences (ESI) investigate flexible film systems. In experiments these flexible film systems were stretched up to strains of 20 % with tensile loading. Such high strains always lead to the formation of cracks and necks in the metal films. Figure 1.3 shows microscope images of the surface of three copper films at high global strains.

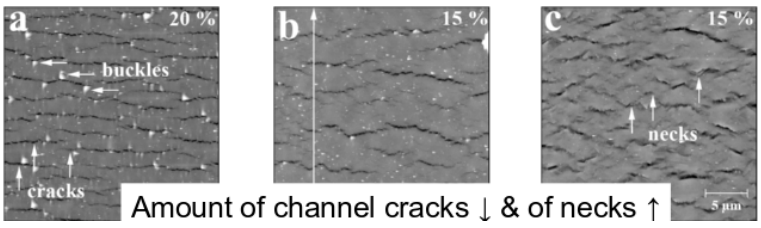

Figure 1.3: Cracks and necks in the copper films in the three different samples. a) shows the 50 nm copper layer, b) the 100 nm copper layer, and c) the 200 nm copper layer. The global strains are displayed in the microscope images. (These pictures are provided by MPIE)

In–situ stress measurements with synchrotron X–ray diffraction were made to obtain stress data in the copper films. This method measures the alteration of the distance between lattice planes in the films. Mechanical stresses have an influence on the distance between lattice planes. Vice versa it is possible to calculate stresses on the basis of the distance between lattice planes [5]. The diagrams in Fig. 1.4a and Fig. 1.4b show the

results of these stress measurements. Also crack and neck densities were determined and they can be found in Fig. 1.4c and Fig. 1.4d. A high dependence of the copper layer thickness on all measured parameters is obvious. The different stress levels at high global

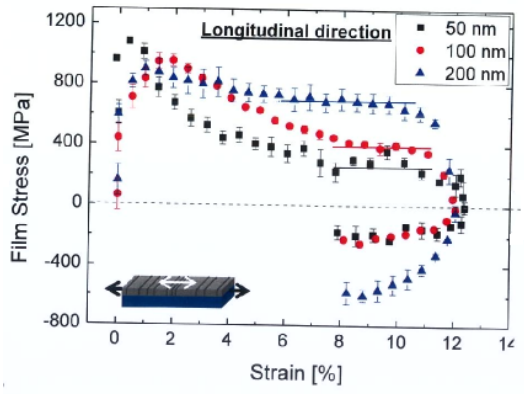

(a) Film stresses in copper in longitudinal direction (x–direction).

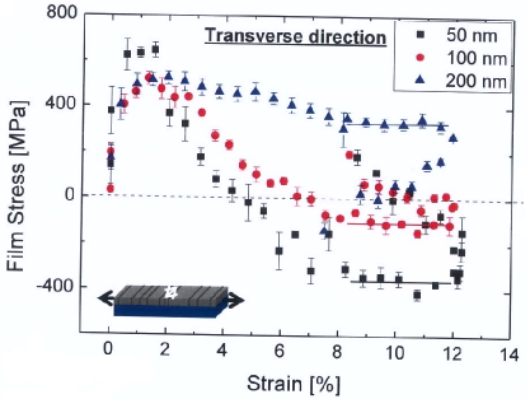

(b) Film stress in copper in transverse direction (z–direction).

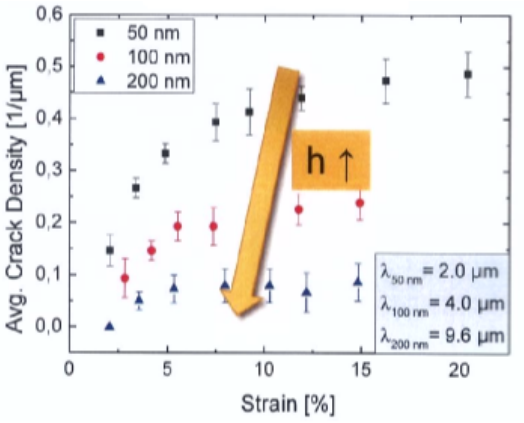

(c) Crack densities in copper.

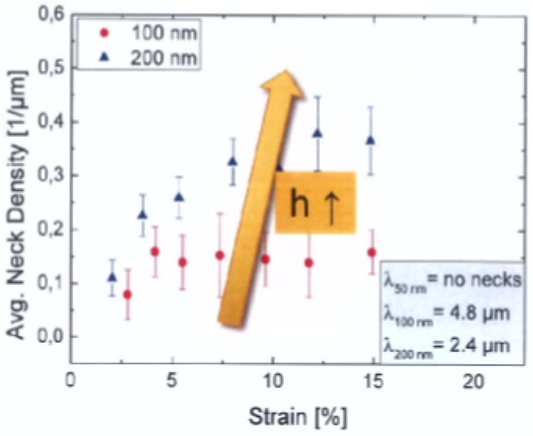

(d) Neck densities in copper.

Figure 1.4: Measurements from flexible film systems with the three investigated copper layer thicknesses 50, 100 and 200 nm. (These pictures are provided by MPIE)

strains in Fig. 1.4a and Fig. 1.4b are very interesting. It is part of this thesis to find the reason for this difference.

Chapter 2

Finite element modelling of the experimental process

All simulations in this thesis were performed with Abaqus [1] and the FE–meshes were designed in Hypermesh [3]. Due to the simulation of cracks and the use of non–linear material laws, non–linear incremental FE–analyses are required. Some special approaches for the localisation and formation of cracks were used in the simulations and will be shown in this chapter.

2.1 Cohesive Zones

One possibility to simulate cracks in a FE–simulation is the usage of cohesive zone elements. These elements are able to model the behaviour of adhesive joints, interfaces in composites and other situations where the integrity and strength of interfaces may be a problem. Abaqus offers different types of these elements. For the simulation of cracks cohesive zone elements were used, which define their constitutive response directly in terms of a traction–separation law [1, 2].

The implemented traction–seperation law in Abaqus assumes initially linear elastic behaviour

$$\begin{bmatrix} t_n \\ t_s \end{bmatrix} = \begin{bmatrix} K_{nn} & 0 \\ 0 & K_{ss} \end{bmatrix} \begin{bmatrix} \epsilon_n \\ \epsilon_s \end{bmatrix}. \tag{2.1}$$

For two dimensional problems the traction stress vector $\mathbf{t}$ consists of two components which represent the normal traction stress t_n and the shear traction stress t_s. The strains ϵ_n and ϵ_s can be defined with the corresponding separations δ_n and δ_s and the original thickness of the cohesive zone element T_0 with

$$\epsilon_n = \frac{\delta_n}{T_0}, \qquad \epsilon_s = \frac{\delta_s}{T_0}. \tag{2.2}$$

It is possible to give this type of element in the model an initial thickness of zero, required for this problem because the cohesive zones mustn't be a spatial part of the model. The cohesive zones enable only the crack formation. The original or constitutive thickness in the background T_0 is by default 1.0. This ensures that the strain is equal to the separation.

After the phase of linear elastic behaviour, if a damage initiation criterion is satisfied, starts the damage process. To determine a damage initiation stress it's required to specify a damage initiation criterion. Abaqus offers a lot of damage initiation criteria but all following simulations use the maximum nominal stress criterion

$$\max \quad \left(\frac{t_n}{t_n^0}, \frac{t_s}{t_s^0} \right) = 1. \tag{2.3}$$

A value of 1 or higher indicates that one of the damage initiation stresses t_n^0 or t_s^0 is reached. This criterion applies only for tensile normal stress t_n. Compressive stress does not lead to a damage initiation.

After satisfaction of the damage initiation criterion the evolution of damage follows. The damage process follows the damage–evolution–law

$$t_n = \begin{cases} (1-D)\ t_{n,el}, & t_{n,el} > 0 \\ t_{n,el}, & \text{otherwise} \end{cases}, \qquad t_s = (1-D)\ t_{s,el}. \tag{2.4}$$

$t_{n,el}$ and $t_{s,el}$ are the traction stress components predicted by the elastic traction–separation behaviour for the current strains without regard to damage. The damage variable D represents the damage progress. It initially has the value zero and increases monotonically to one after the damage initiation criterion is reached. The damage variable D allows to implement different softening behaviours in the phase of damage evolution. Examples are

linear softening or exponential softening, but also individual softening behaviours can be implemented in Abaqus.

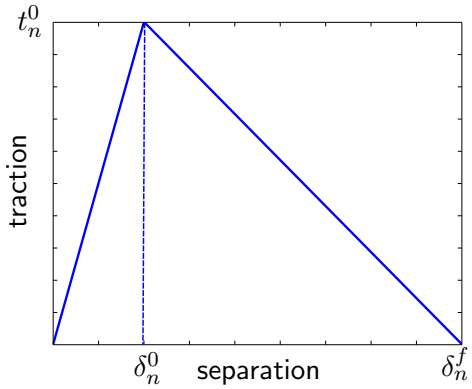

Figure 2.1: Traction–separation law with linear softening for normal stresses.

Figure 2.1 shows a traction–separation law with linear softening. A damage–evolution law with linear softening needs only the separation at complete failure δ_n^f. The area under the damage evolution part of the traction–separation–law

$$\frac{t_n^0 \left(\delta_n^f - \delta_n^0\right)}{2} \tag{2.5}$$

represents the fracture energy density in terms of energy per unit area. Therefore, the amount of δ_n^f decides if the material is rather brittle or ductile.

Cohesive zone elements which define their constitutive response directly in terms of a traction separation law always use nominal stresses and not Cauchy stresses (true stresses). So it is not possible to make geometric non–linear computations. Otherwise two different stress measures would be used in the computations. So the geometric linear computation is a further assumption in the model.

2.2 Finite Element Model

For the computation of the film cracking a 2D–model is sufficient. To consider also transverse effects in the model a generalized plain strain state is required. So this model represents the middle plane of the three dimensional film system. A further assumption is a perfect interface between the polyimide substrate and the chrome film and between

the chrome and copper film. The length of the entire model in x–direction is 20 μm. The generalized plain strain elements need an out of plane width which was chosen to be 10 mm. Thus, a slice of 10 mm thickness is considered in z–direction.

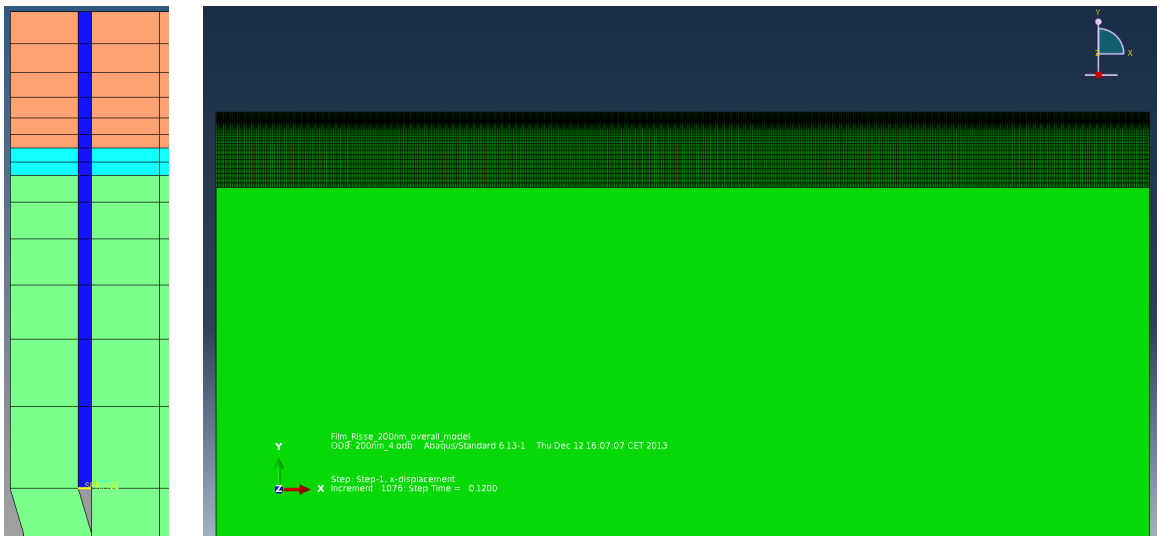

(a) One cohesive zone

(b) Entire FE–mesh with the fine mesh in the upper part of the model and one big element in the lower part of the model.

Figure 2.2: Entire FE–mesh with a detail from one cohesive zone.

The FE–model includes 2D continuum elements and cohesive zone elements. The cohesive zone elements enable the formation of cracks. Generalized plain strain elements with quadratic interpolation and eight nodes were chosen. The model is built by pairs of generalized plain strain elements separated from it's neighbouring pairs by a cohesive zone. Each cohesive zone is located in copper, chrome and partially in polyimide. Figure 2.2a shows such a cohesive zone between two continuum elements. The blue stripe is only for illustration because the thickness of the cohesive zone is zero. The model is discretized by 800 elements along the length in x–direction (Fig. 2.2b). It has 400 cohesive zones allowing a crack appearance at the respective points. Abaqus offers only cohesive zone elements with four nodes and not with six. Since the distribution of node forces of quadratic interpolated continuum elements is not constant, the combination of two cohesive zone elements with one quadratic interpolated continuum element is not consistent (Fig. 2.3a). Therefore a multi point constraint (MPC) is used to link the three nodes of the quadratic interpolated continuum element at the edge which is linked with the cohesive zone element (Fig. 2.3b). This multi point constraint ensures that these three nodes lie always on one

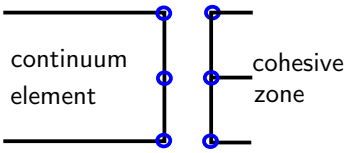

(a) Combination of two cohesive zone elements with one quadratic interpolated continuum element.

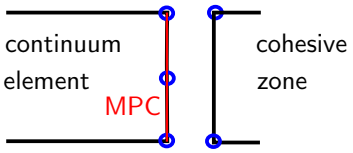

(b) Combination of one cohesive zone element with one quadratic interpolated continuum element by the help of a MPC.

Figure 2.3: Combination of quadratic interpolated continuum elements with cohesive zone elements.

straight. This approach is used in all material layers.

The cohesive zone in polyimide is essential to enable the opening of the cohesive zone in chrome at the interface to polyimide. But the cohesive zone in polyimide does not go through the whole polyimide sublayer. Only the first six polyimide elements are separated by a cohesive zone element and so an ending of the cohesive zone in polyimide is required. Therefore the last two nodes of the sixth cohesive zone element are linked Fig. 2.2a by a constraint.

Figure 2.2b shows a fine mesh in the upper area of the model. This part includes the respective copper layer, the 10 nm chrome layer and 2 μm of the polyimide sublayer. But the polyimide sublayer has a thickness of 50 μm. A computation of the entire model with a mesh fineness like in the upper part would be numerically very expensive. Since generalized plain strain elements are used the modelling of the entire polyimide is absolutely necessary. Otherwise the transverse stresses wouldn't be correct. So the lower part consists of one big polyimide element only. That is acceptable because all the bending stresses are substantially subsided in this area and the strain energy under pure tensile loading is the same as it would be in a finer mesh.

2.3 Statistical distribution of material parameters

As mentioned there are 400 cohesive zones in the FE-model. Under tensile loading, before the first crack appears, the stress state in every material layer is homogeneous. When the damage initiation criterion is fulfilled in one of the material layers, every cohesive zone in this layer would begin with damaging. Certainly, this is compared to experimental

observations not realistic. The formation of cracks starts with a single crack formation at the weakest position and continues in a process, in which the crack density grows monotonically up to saturation. In order to simulate this process, the damage initiation values in the chrome and copper cohesive zones are statistically distributed perturbing the homogeneity of crack probability similarly to the introduction of imperfection in a bifurcation analysis. These are calculated with

$$\sigma_{DI,i,m} = \sigma_{u,m} + s_m \; n_i. \tag{2.6}$$

In this formula $\sigma_{DI,i,m}$ represents the statistically distributed damage initiation stress in the cohesive zone i in material m and $\sigma_{u,m}$ represents the ultimate stress in material m. m stands either for copper or for chrome. s_m is a standard degression, which is 5 to 10 percent of the ultimate stress. n_i represents a value out of a normal distributed sample to bring in the statistical character.

Chapter 3

Film system with a 50 nm copper layer

The first investigations were made with the film system with a 50 nm thick copper layer, because here more information about material parameters were available than in the two other film systems. Another important fact in this film system is that every crack runs through both metal films. Figure 3.1 shows this fact at a global strain of 12 %. This circumstance simplifies the first computations, because the estimated material parameters can be checked by only one experimental data, namely the crack density.

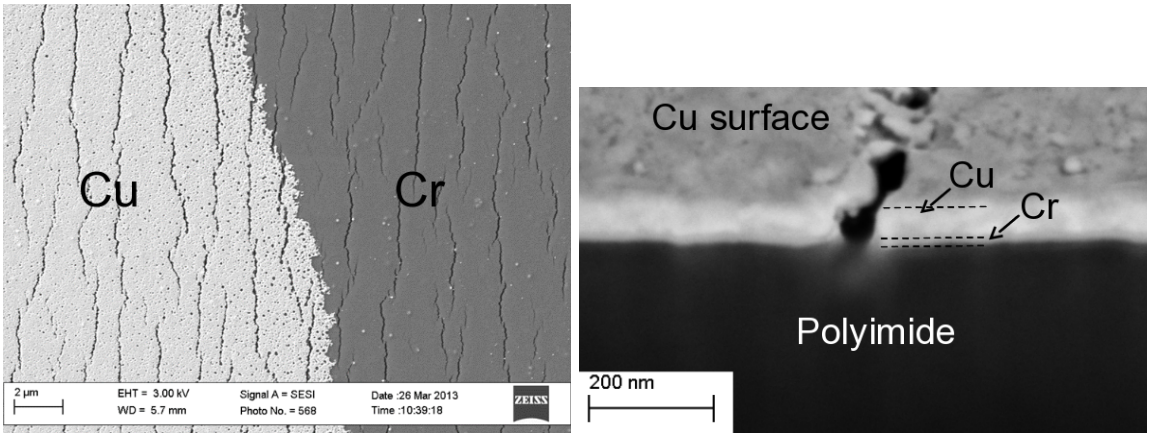

(a) Picture of channel cracks which run through copper and chrome. The copper layer is etched away in the right part.

(b) FIB (Focused Ion Beam) cross section through a crack.

Figure 3.1: Experimental foundation for the proposition that all cracks run through chrome and copper. (These pictures are provided by MPIE)

3.1 Material laws in the model

The assumed material parameters and behaviours are explained in this section. Because of the small layer thicknesses associated with the morphology in chrome and copper films, the material parameters and their behaviours are not comparable with those of bulk materials. But finding material parameters and behaviours of such thin metal films is not easy. So, another goal of the computations is to find suitable material parameters which lead to results comparable with the experiments in Chapter 1.2. This is performed by the variation of material parameters in parameter studies.

3.1.1 Material properties in Copper

A v.Mises elastic–plastic material law with $E = 120\,GPa$ and linear hardening with $E_T = 1100\,MPa$ is used for the 50 nm film model (Fig. 3.2). Similar material data can be found in [8]. These data seems feasible, because the measurements showed a comparable yield limit and hardening behaviour (Fig. 3.13a). The yield limit amounts to 1100 MPa and the Poisson's number ν is 0.3. The ultimate stress $\sigma_{u,cu}$ is a parameter which has to be varied in order to achieve correspondence between our model and experiments (Chapter 2.3) .

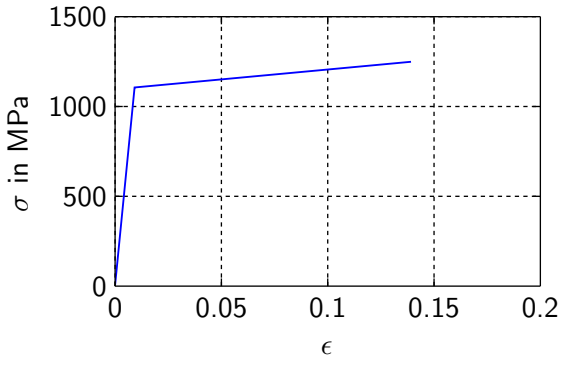

Figure 3.2: True stress – logarithmic strain curve for copper.

3.1.2 Material properties in Chrome

For chrome a purely elastic material law with a ultimate strain of about 4 % is assumed. This is based on the assumption that hardening does not occur in such thin metal films.

The Young's modulus amounts to E=279 GPa and the Poisson's number ν is 0.21.

3.1.3 Material properties in Polyimide

For polyimide v.Mises plasticity is assumed, too. The material's stress–strain diagram is shown by the blue curve in Fig. 3.3, with a calculated Young's modulus of E=3.704 GPa. A Poisson's number of $\nu = 0.37$ is used. The green curve represents the true stress–effective plastic strain curve, which is required from Abaqus to provide data for the v.Mises plasticity.

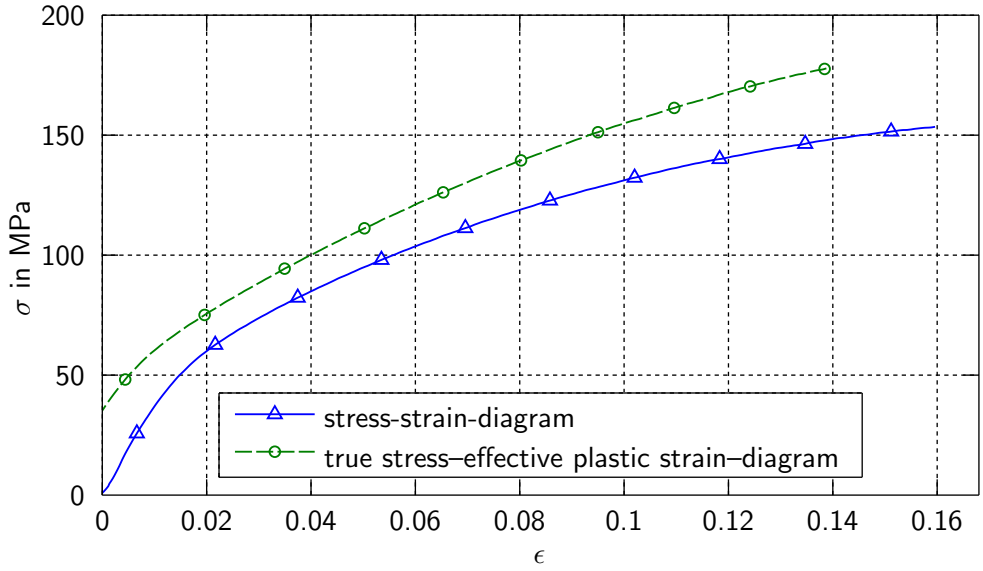

Figure 3.3: Polyimide material data for the material input in Abaqus

3.2 Definition of the cohesive zones in the model

3.2.1 Cohesive zones in copper

For the adjustment and evaluation of cohesive zone elements test models are used. In Fig. 3.4a one can see the traction–separation law from a test model for the copper film computed by Abaqus. The maximum normal stress value in this diagram represents the damage initiation value. When this traction is reached, the damage process in the cohesive zone starts. As long as the normal stress has not reached the damage initiation value,

the stiffness of the cohesive zone is extremely high, in order to prevent the model from unwanted stiffness loss at regions where no cracks are formed. One can calculate the stress in the linear elastic part of the traction–separation law with

$$\sigma = K\, u. \tag{3.1}$$

K is the stiffness per unit area of the cohesive zone. Tensile loading leads to a homogeneous stress state σ e.g. in copper at a current global strain ϵ. But which stiffness is useful for the model of the flexible film system? The displacement u of the right face of the film system can be calculated by

$$L\,\epsilon = \frac{800\, l_E\, \sigma}{E} + \frac{400\, \sigma}{K}, \tag{3.2}$$

were L is the entire model length in x–direction, ϵ is the longitudinal global strain and l_E is the length of one continuum element (they all have the same length of 25 nm). As mentioned before, the model length is discretized by 800 continuum elements and 400 cohesive zone elements. The first part on the right side, which represents the sum of the continuum element displacements, in this equation should be a lot larger than the second part, which represents the sum of the cohesive element separations. These considerations lead to the relationship

$$K >> \frac{E}{2l_E}. \tag{3.3}$$

For K=1000000 GPa the sum of the separations of the 400 cohesive zones is only about 0.02 % of the entire displacement in x–direction. Therefore, the elastic material behaviour is represented by a nearly vertical line in Fig. 3.4a.

In the second phase, after reaching the damage initiation criterion, the stress level in the cohesive zone decreases and the damage value goes from zero to one. When the damage value is one, the cohesive zone element is no longer able to transfer any loading and the element disappears. The area under the traction-separation curve represents the fracture energy density. That is the dissipated energy as a result of the fracture process. This energy is an important parameter for the simulation. For the 50 nm film model a relatively small fracture energy density is chosen, so the material behaviour is assumed as rather brittle. Figure 3.4a shows this brittle material behaviour. The separation of complete

failure δ_n^f is only about 0.6 nm. That means, the cohesive zone breaks down, when the relative displacement of the two neighbouring continuum elements reaches 0.6 nm. Such a low value is chosen because fracture of such thin films is rather brittle. This choice is also practicable to avoid the influence of fracture energy in the first parameter studies in order to keep the amount of varied parameters low. Figure 3.4b shows the computed stress-strain behaviour in a copper element next to the cohesive zone element resulting from these assumptions.

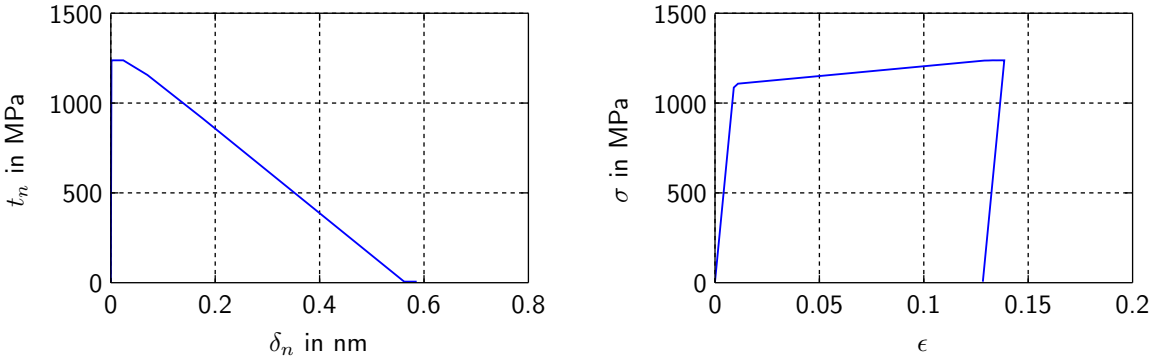

(a) Traction–separation law in the cohesive zone (b) Stress – Strain diagram in the bulk material

Figure 3.4: Test results in the cohesive zone in copper.

3.2.2 Cohesive zones in chrome

The cohesive zones in chrome have basically the same behaviour as the cohesive zones in copper. Of course the parameters for stiffness and damage initiation are different. The stiffness K is in the same proportion to E as in copper (if this is not the case shear stresses occur in the model caused by different separations in the different films) and the damage initiation corresponds to a ultimate strain of about 4 %. As mentioned in Chapter 1 chrome is a brittle interface layer and the separation of complete failure δ_n^f is equal to the one in copper.

3.2.3 Cohesive zones in polyimide

The cohesive zone in polyimide has completely different properties as compared to the cohesive zones in copper and chrome. In polyimde the cohesive zone is essential to enable

the crack opening. However, a damage process (reduction of the bearable stress in the cohesive zone) or a crack formation must not start there but large local strains should be able. Figure 3.5a shows the traction-separation law in polyimide. One can see a horizontal line in phase two after reaching the damage initiation stress. So the stress level t_n remains constant and the damage value is computed with

$$D = 1 - \frac{t_n}{t_{n,el}} = 1 - \frac{t_n}{K_{nn}\,\delta_n} \tag{3.4}$$

This equation follows with the assumption of a constant traction t_n in the damage evolution part (Eq. 2.4). This cohesive zone enables the required large local strains in polyimide at the positions of chrome cracks at a constant stress level. Figure 3.5b shows the computed stress–strain behaviour in a polyimide element next to the cohesive zone. This figure shows that the extremely high strains in the neighbouring cohesive zones have no influence on the stress–strain behaviour in the 2D continuum elements.

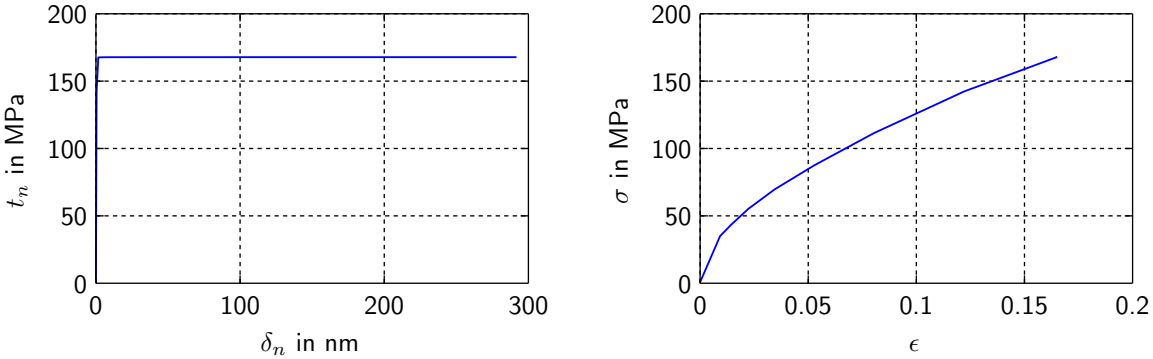

(a) Traction – Seperation law in the cohesive zone (b) Stress – Strain diagram in the 2D continuum elements

Figure 3.5: Test results for the cohesive zone in polyimide.

3.3 Results from FE–analyses

All FE–Analyses are displacement controlled and the application of the displacement is performed incrementally till 12 % of the model length. It is important to use a first strain increment that is in the linear elastic part of all material laws in the model. Otherwise it is not possible to find the right equilibrium.

3.3.1 New findings shown in a specific simulation

Figure 3.6 shows the flexible film system at a global strain of 12 % for a model in which the mean damage initiation stress in chrome is chosen to be $\sigma_{u,cr} = 12000\,MPa$ and in copper $\sigma_{u,cu} = 1243\,MPa$. These parameters apply in the following descriptions until new ones are defined. The figure shows eight cracks in chrome and copper, and the v.Mises stress in polyimide is displayed by coloured fringes. The cracks don't appear simultaneously, they appear one after another. The positions are defined by the statistical distribution of the damage initiation stresses. There are no chrome cracks only. All are running through chrome and copper. At first the crack formation will be shown. Crack formation always follows the same procedure. To demonstrate this process, the first crack in this simulation is chosen.

Figure 3.6: Overall model with the resulting cracks at a global strain of 12 %.

All stresses in the fringeplots in Fig. 3.8 are longitudinal stresses (S11). Figure 3.7 shows the stress levels for the fringeplots in Fig. 3.8 so that stress levels can be assigned to the colors in the fringeplots. Each type of blue area in these fringeplots is an area of compressive stress in longitudinal direction. These stress values are given in $N/\mu\,m^2$. Multiplying with 10^6 results in N/mm^2.

Up to a certain global strain of about 3.1 % the stress state in all three layers in the model is homogeneous (Fig. 3.8a). Since the material behaviour in chrome is just elastic with a high Young's modulus, the stress level in chrome reaches the damage initiation stress at first (Fig. 3.8b). It is important that, with the above specified material parameters, the crack formation starts always in the chrome layer. After chrome is broken, this layer undergoes elastic spring back. This spring back is stronger the higher the damage initiation stress in chrome is. Due to the crack opening in chrome, an area of stress concentration is induced in copper and in polyimide. Figure 3.8c shows the broken chrome with partially damaged copper and polyimide. A comparison of the four fringeplots in Fig. 3.8 shows the unloading of the chrome layer within the copper layer increasing crack

width. Due to the spring back process of chrome, areas of compressive stress nearby the chrome layer can be seen already.

So from this part of the simulation we have learned that the damage initiation stress of chrome is responsible for the global strain level, at which the first crack appears. The $\sigma_{DI,cr}$ values are also relevant for the development of the crack density, i.e. it strongly influences the distance between two cracks at a certain global strain. The higher the damage initiation stress is, the larger is the distance between two cracks. It is important to mention that due to the elastic spring back chrome can induce compressive stress states in the broken copper film.

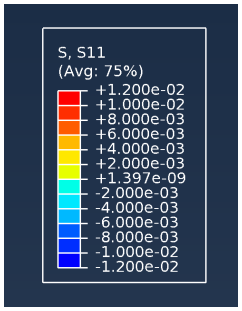

Figure 3.7: Longitudinal stress levels for the fringeplots in Fig. 3.8 (maximum value is the mean damage initiation stress in chrome $\sigma_{u,cr}$).

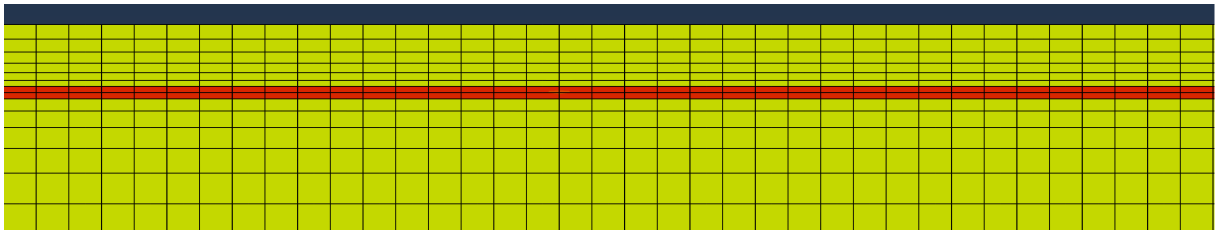

(a) Homogeneous stress state (longitudinal stress) in all 3 layers at a global strain of 3.1239 %.

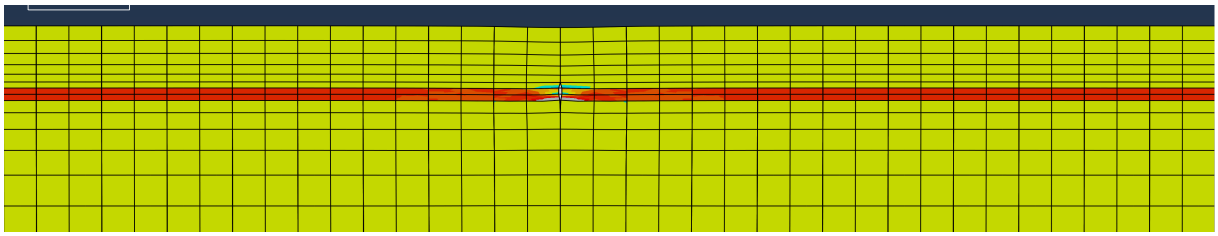

(b) Start of crack formation at a global strain of 3.1317 %.

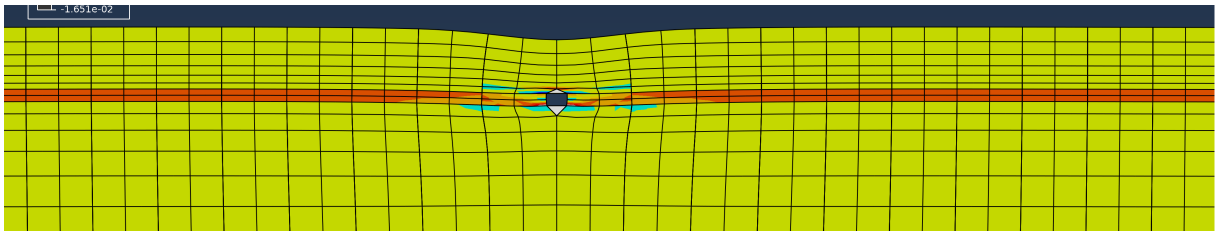

(c) Crack through whole chrome layer at a global strain of 3.1329 %.

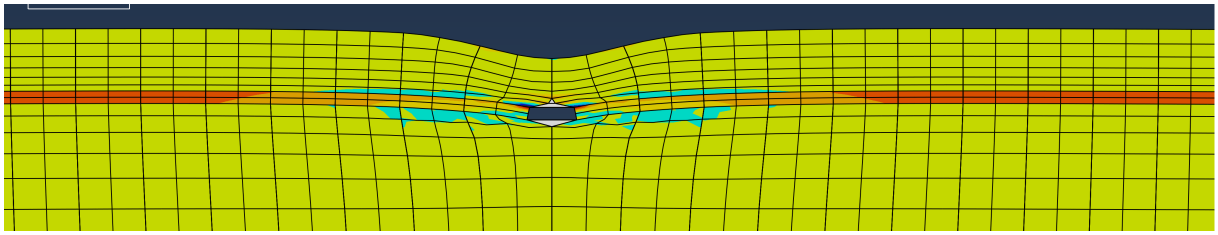

(d) Start of crack formation in copper at a global strain of 3.1385 %.

Figure 3.8: Plots of longitudinal stress with the crack formation in chrome.

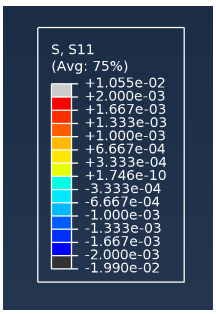

Figure 3.9: Longitudinal stress levels for the fringeplots in Fig. 3.10 for better presentation of the stress field in copper

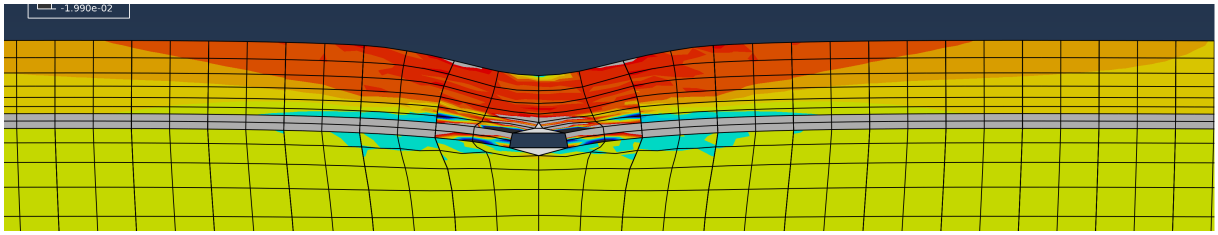

(a) Start of crack formation in copper at a global strain of 3.1385 %.

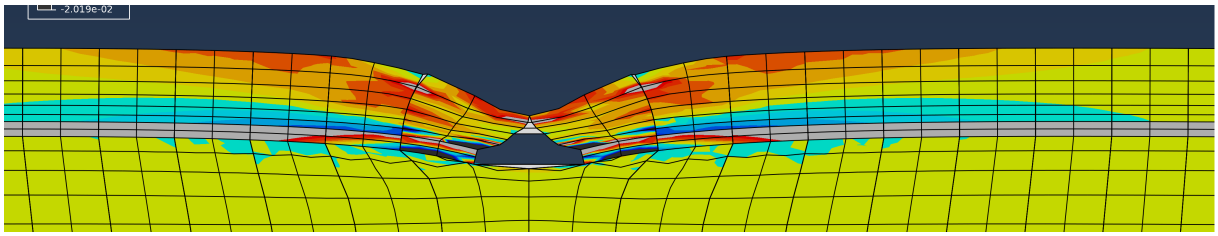

(b) crack propagation through copper at a global strain of 3.1509 %.

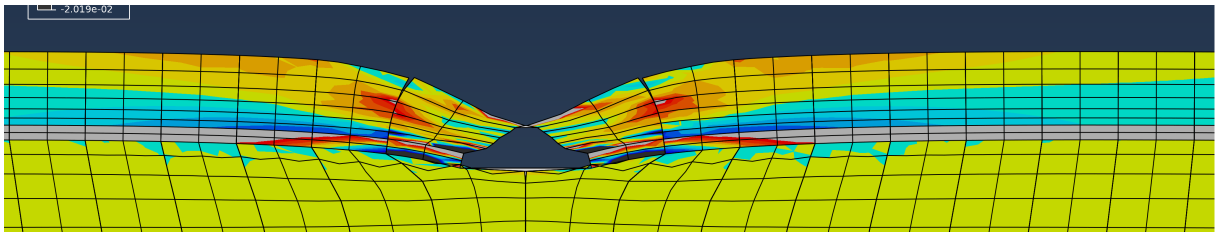

(c) Nearly cracked copper layer at a strain of 3.1598 %.

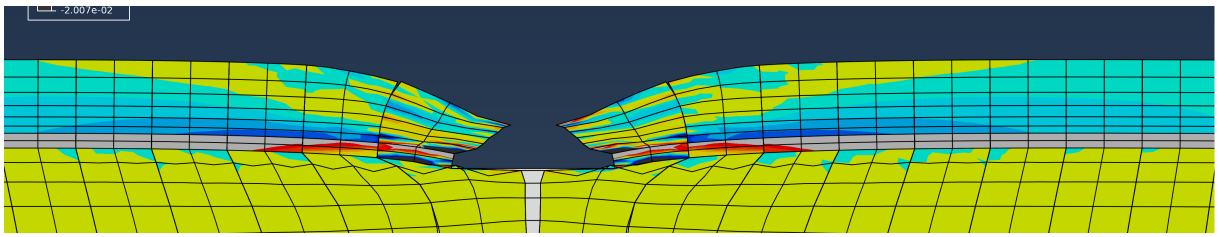

(d) Crack opening at a strain of 3.2287 %.

Figure 3.10: Plots of longitudinal stress with the crack formation in copper.

Figure 3.10a shows the situation at the same global strain as in Fig. 3.8d but with the stress levels in Fig. 3.9. The fringeplot Fig. 3.10a shows a stress reduction with increasing distance from the crack, being a result of the spring back of the chrome layer. The copper layer is not yet broken and has undergone large plastic deformations. The load transfer between chrome and copper layers is due to in-plane shear. A kind of shear lag appears between chrome and copper and another shear lag is joined between chrome and polyimide. This shear lag is attenuated far away from the crack and the stress state there is again almost homogeneous in each layer. The other fringeplots in Fig. 3.10 show the propagation of the crack in copper. They also show the increase of the compressive stresses in copper while the crack goes through copper. When looking at a piece of the chrome and copper film between neighbouring cracks one finds that, due to plastic deformations, the copper layer has became longer than the chrome layer, which has pure elastic material behaviour. Therefore, also after completion of the cracking process the shear lag is responsible for the compressive stress state in copper between neighbouring cracks.

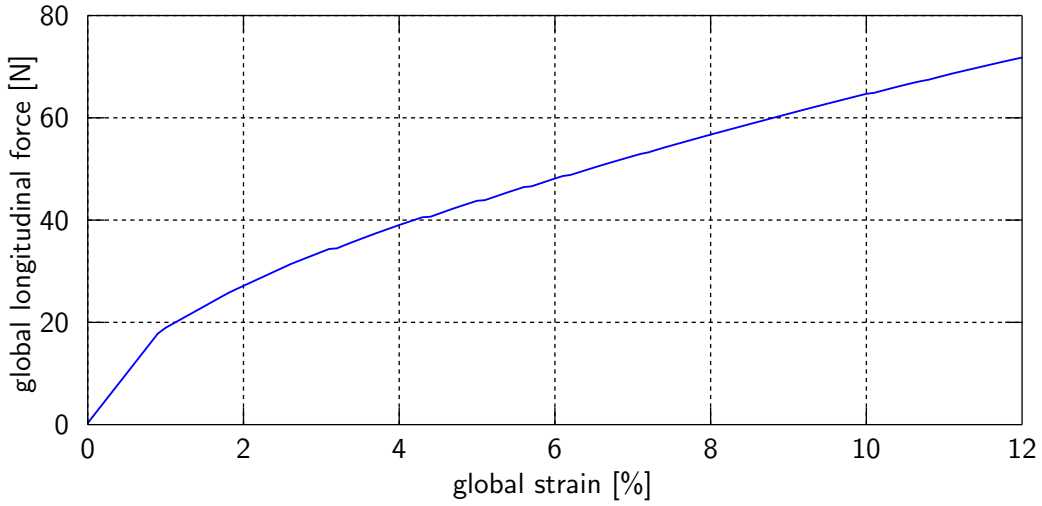

Figure 3.11: Global force – global strain diagram.

The diagram in Fig. 3.11 shows the global longitudinal force dependent on the global strain. The cracks can be identified by small edges in the line. They are so small because the force in the polyimide sublayer dominates the contributions to global force. Although the Young's modulus is comparatively small. It is the extremely larger thickness of this

layer, which results in this domination.

In the experiments volume averaged stresses in copper films have been determined instead of local stress values (Chapter 1). Thus, mean stress values in the copper layer were calculated from the computed stress distribution for every global strain state. The used finite elements have four integration points, in which one obtains the respective stress values. The element size in the entire copper layer is not constant. So, it is necessary to build element size weighted mean stress values in every element before one can build the volume averaged mean stress in the entire copper. These mean stress values were built

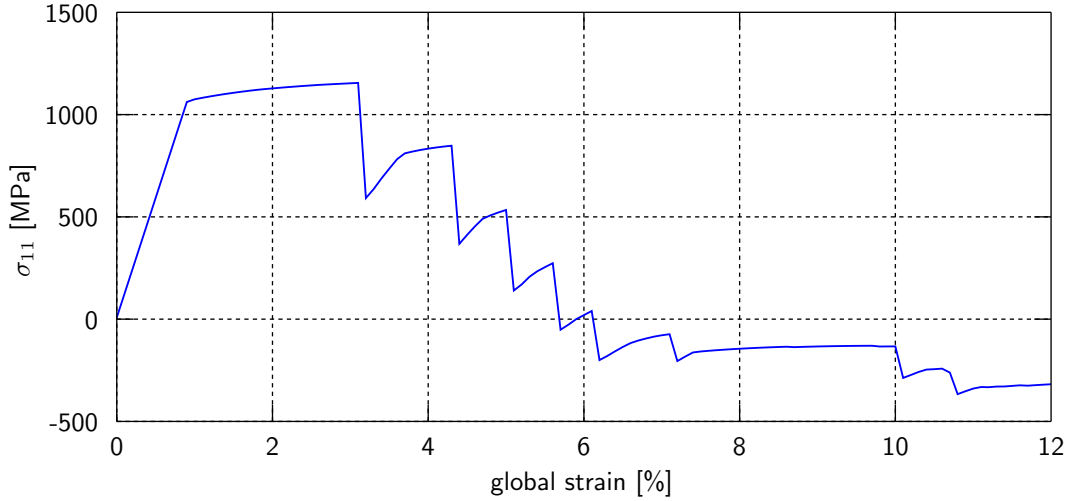

(a) Mean stress in longitudinal direction in copper.

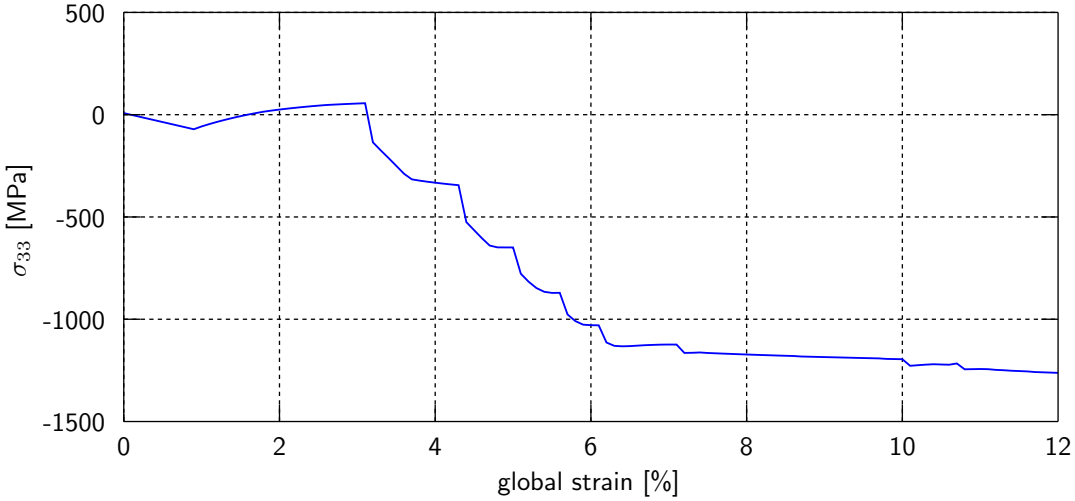

(b) Mean stress in transverse direction in copper.

Figure 3.12: Mean stresses in longitudinal and transverse direction, respectively

for every global strain state by

$$\sigma_{11,cu,t} = \frac{\sum_{j=1}^{N} \frac{\sum_{i=1}^{n} \sigma_{11,i,j,t}}{n} A_j}{A_{ges}}, \tag{3.5}$$

where the variables are defined as:

- t: global strain level
- n: number of integration points in one 2D–continuum–element (n=4)
- N: number of elements in entire copper (different for the three layer thicknesses 50 nm, 100 nm and 200 nm)
- $\sigma_{11,cu,t}$: mean stress in longitudinal direction at global strain t
- $\sigma_{11,i,j,t}$: stress in longitudinal direction in the integration point i, element j and global strain t
- A_j area of element j
- A_{ges} entire area of the copper layer

The same applies to the transverse stress σ_{33}. The dependence of these mean stress values on the global strain can be found in Fig. 3.12. For comparison the measured results are pictured in Fig. 3.13. Figure 3.12a shows the averaged stress values, called mean stresses, in longitudinal direction in the whole copper layer. The development of the longitudinal stresses is qualitatively comparable. The major differences are the global strain at which the first crack appears and the mean stress level in copper after 5 % global strain. As described above, the damage initiation stress of chrome is a very important parameter. This value defines the global strain value at which the first crack appears and it also influences the number of cracks in chrome and, therefore, also in copper. The stress state at high strains is also influenced by the hardening parameters in copper.

Figure 3.12b shows the mean stress in the whole copper in transverse direction. This figure is not comparable with the measurements. But with these measured results in Fig. 3.13b we have to be careful. Based on the Poisson's effect there should be a compressive stress state in transverse direction, at least as long as the material behaviour is

linear in the three layers. The results from the FE simulation show this compressive stress state, where the measured ones show tensile stresses.

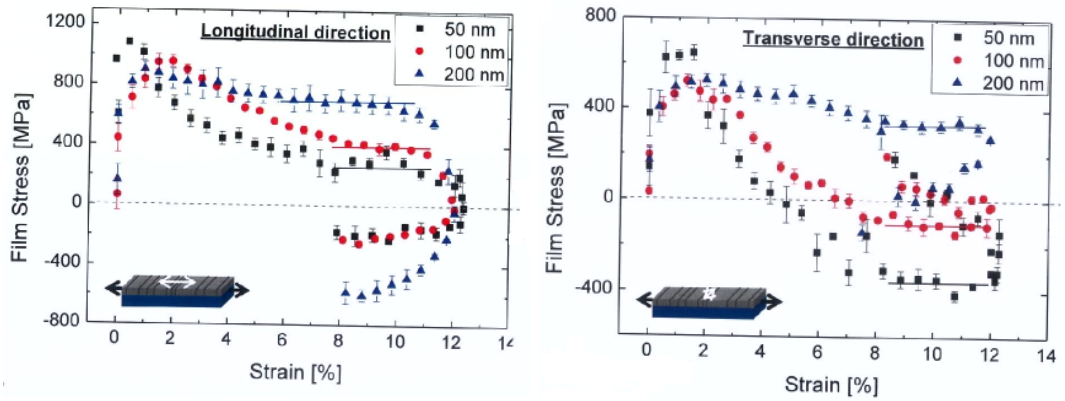

(a) Longitudinal direction (b) Transverse direction

Figure 3.13: Measured copper film stresses in longitudinal and transverse direction for the three copper films provided by MPIE.

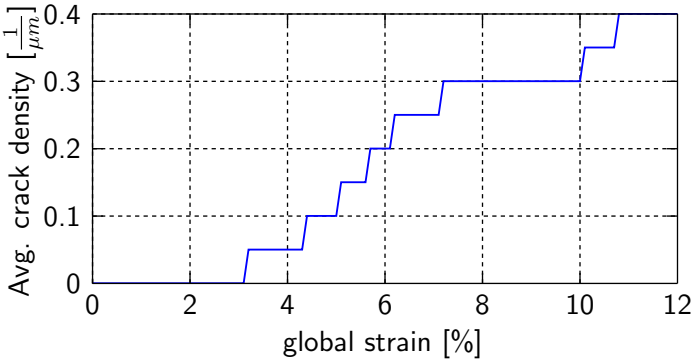

Figure 3.14: Computed average crack density dependent on the global strain.

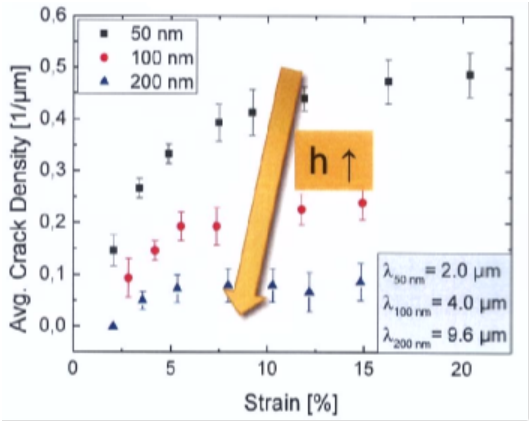

Figure 3.15: Average crack densities for the three copper layers from experiments provided by MPIE.

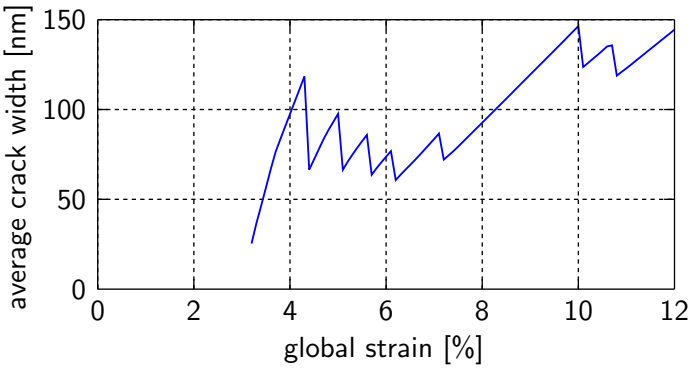

Figure 3.16: Computed average crack width dependent on the global strain.

Figure 3.14 shows the computed average crack density. This matches well with the measurements in Fig. 3.15. A crack is counted as a crack in Fig. 3.14 only if the cohesive zone element at the top of the copper layer is terminated. That's the case, when the current separation δ_n in the cohesive zone element is larger than the separation of complete failure δ_n^f in the damage evolution law. The major difference between computations and measurements is the global strain at which the first crack appears, as already mentioned. Figure 3.15 shows that the crack density has not reached a saturated value at a global strain of 12 %.

Figure 3.16 shows the computed average crack width at different global strain values. These values are smaller than the measured ones in Tab. 3.1. The crack width has an influence on stress levels at high global strains and also on the crack density. The averaged longitudinal strain in the copper film between two cracks is lower than the global strain. Reason for this is, that the sum of the crack widths is part of the global displacement

and, therefore, the averaged copper strain between two cracks is reduced. So the crack width is an important factor which influences the crack density and is part of further investigations.

average crack width [nm]	distance between cracks [μm]	global strain [%]
185 +/- 49	3.01 +/- 1.2	5
257 +/- 64	2.29 +/- 0.75	12
295 +/- 74	1.999 +/- 0.65	20

Table 3.1: Measurements of average crack widths and distances between cracks at different global strains.

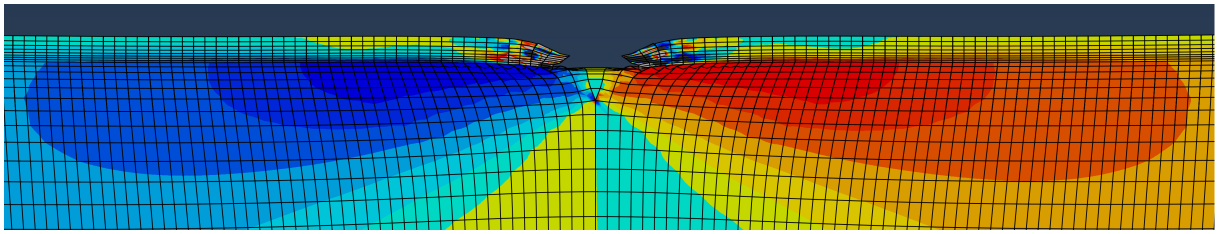

(a) Shear stress after the formation of the first crack.

(b) Shear stress at the end of the simulation at a global strain of 12 %

Figure 3.17: Plots of longitudinal stress with the crack formation in copper.

Figure 3.18 shows the in–plane shear stress in polyimide (S12) at the interface to chrome after the formation of the first and the last crack. This shear stress distribution represents the shear lag in the interface between chrome and polyimide. The x-axis defines the position in the model (the model is 20 μm long). On every jump location is a crack in the model. The three curves in the figures show the shear stress distribution just before a crack appears, at crack opening and just after complete crack opening. Figure 3.17a shows the shear stress in the flexible film system after the first crack and Fig. 3.17b at the end of the simulation at 12 % global strain. Figure 3.17b shows more or less the same as Fig. 3.18b. Every crack is a jump location of the in–plane shear stress.

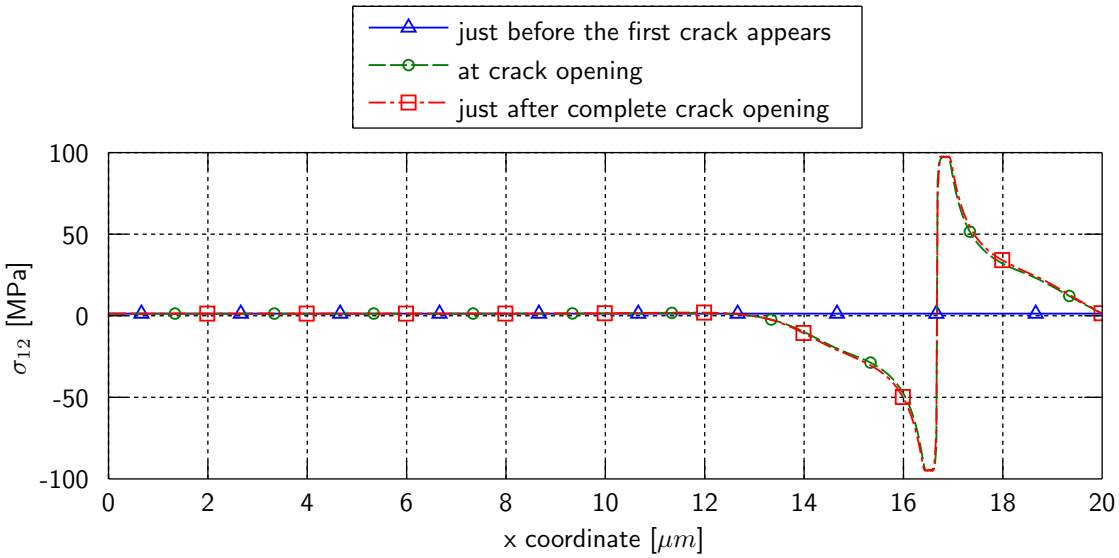

(a) In-plane shear stress in polyimide at the interface to chrome at the first crack.

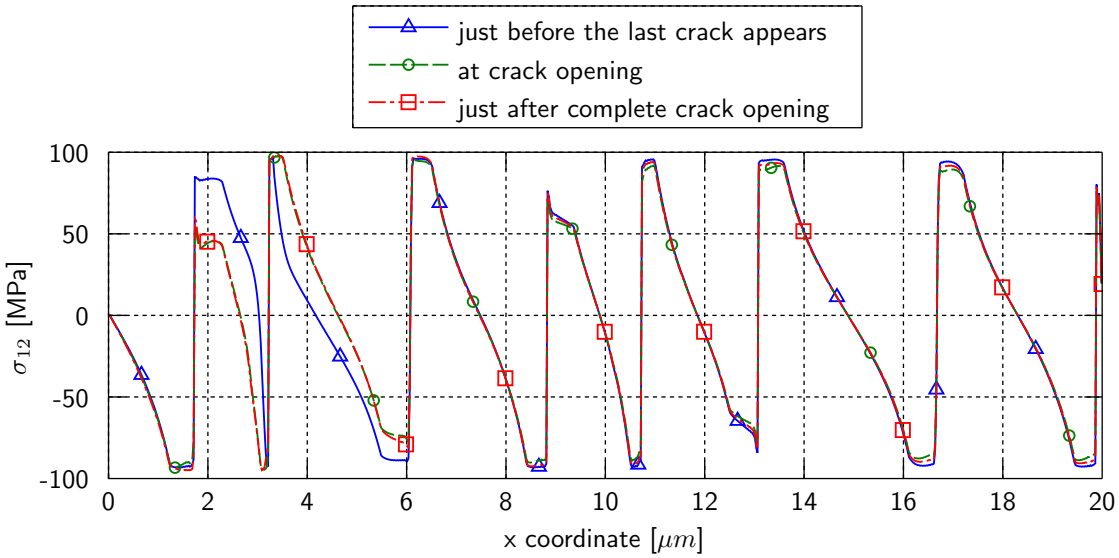

(b) In-plane shear stress in polyimide at the interface to chrome at the last crack.

Figure 3.18: In-plane shear stresses.

3.3.2 Summarized results from several parameter studies

In order to illustrate the influence of the various parameters, several parameter studies were made. Selected results are shown in the figures Fig. 3.19, Fig. 3.21, Fig. 3.22 and Fig. 3.23 for comparison reasons. There a lot more studies were made, but these six studies show the influences quite well. Not all parameters were changed in these studies. The samples out of a normal distribution for the calculation of the damage initiation stresses in copper and chrome are the same in all of these studies. Reason for that is the comparability of the crack locations in x–direction. Certainly, all of these four figures are based on the same parameter sets. The blue curve in the following figures represents results of the previously discussed simulation. The variables in the figure legends have the following meaning:

- $\sigma^0_{y,cu}$ is the yield limit in copper
- $\sigma_{DI,cu}$ is the mean damage initiation stress in copper
- $\sigma_{DI,cr}$ is the mean damage initiation stress in chrome

Since, according to the assumptions chosen in the model, copper hardens linearly, the damage initiation stress and the corresponding strain are directly depended on each other.

$$\epsilon_{DI,cu} = [\frac{\sigma^0_y}{E_{cu}} + \frac{(\sigma_{DI,cu} - \sigma^0_y)}{\sigma^0_y}] \times 100 \tag{3.6}$$

This formula is for the mean values and not for the statistically distributed values. This results in a damage initiation strain in copper of approximately 14 % for the simulation to which all the graphs are assigned, except the cyan. The cyan graph has been achieved for a damage initiation strain in copper of 4 %.

Figure 3.19 shows the comparison of the mean longitudinal stresses in copper. Of course, in every simulation the linear part is equal and the yield limits are comparable with the given material data. Then the hardening part in copper follows and the first crack appears. Remarkable is that for equal damage initiation strains in copper and equal damage initiation stresses in chrome the global strain at the first crack is also equal. There is no dependence from the yield limit. Of course, if the yield limit is too low, copper breaks

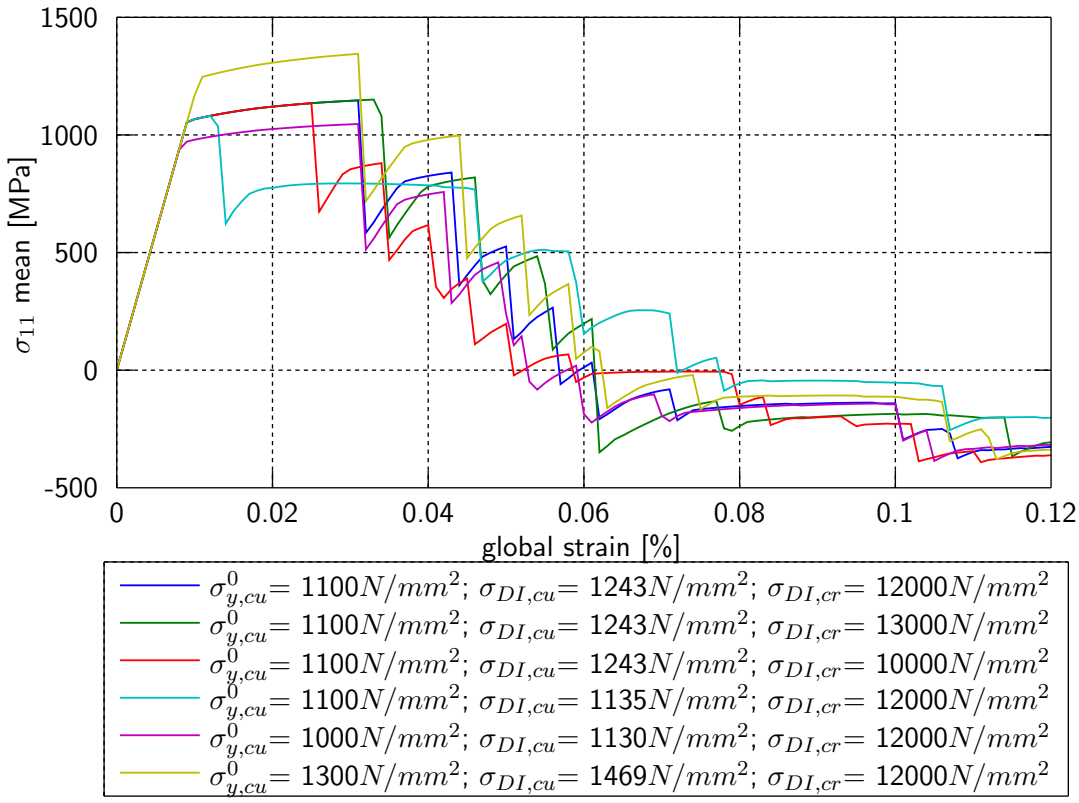

Figure 3.19: Mean stresses in longitudinal direction in copper from several parameter studies.

first. The importance of the chrome damage initiation stress was mentioned already. The cyan graph shows that also the copper damage initiation has an influence on the global strain at which the first crack appears. However, in this simulation copper was broken at first and due to stress concentration at the crack tip a crack in chrome occurs. (Fig. 3.20, limits are shown in Fig. 3.9). This simulation with a lower copper ultimate strain shows also that the ultimate strain, respectively the plastic strain due to plastic deformations is responsible for the compressive stress state in copper at high global strains. The compressive stress state is much more distinct in simulations with higher ultimate strains in copper.

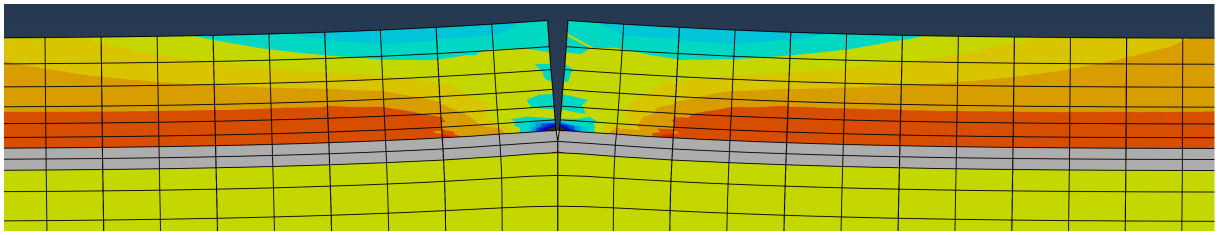

(a) Start of crack formation in copper at a global strain of 1.3 %.

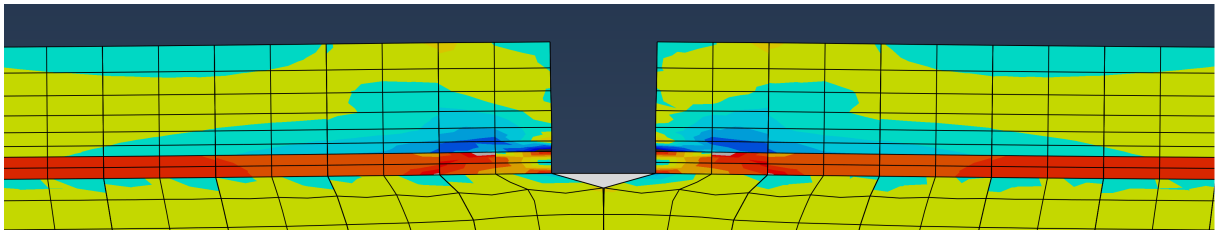

(b) Crack through copper and chrome at a global strain of 1.4 %.

Figure 3.20: Plots of cracks and longitudinal stresses with a damage initiation strain in copper of 4 %

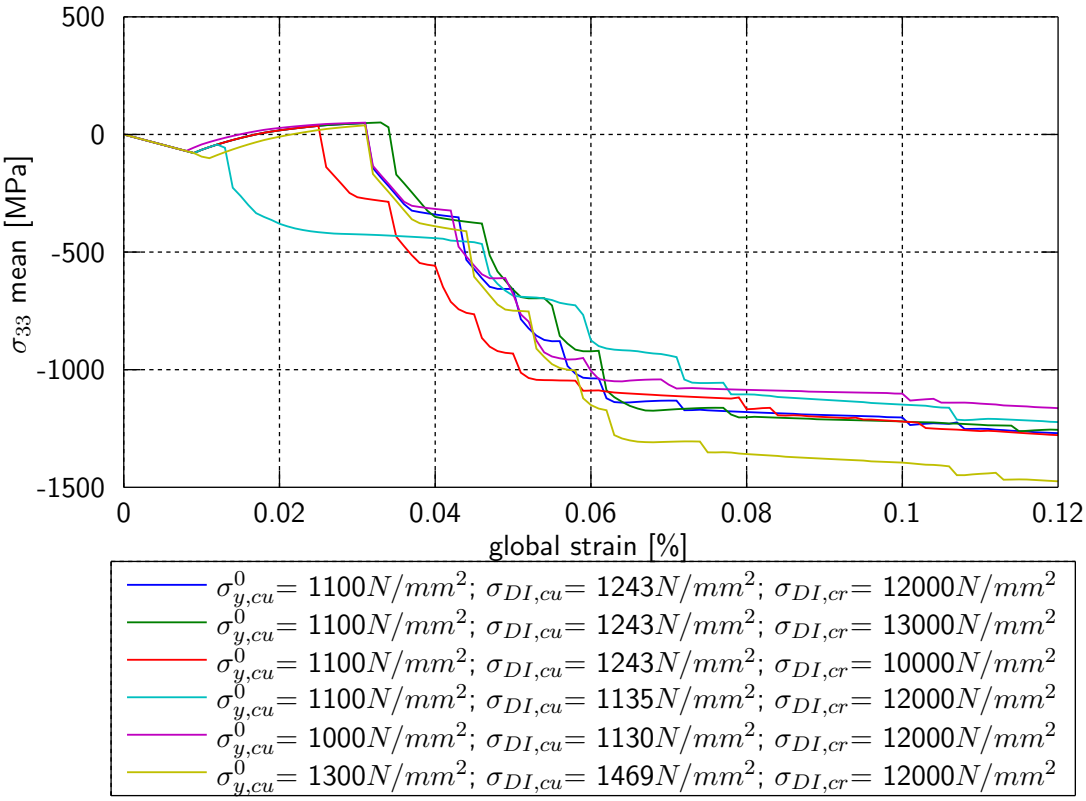

Figure 3.21: Mean stresses in transverse direction in copper from several parameter studies.

In Fig. 3.21 the mean transverse stress in copper is shown as a function of global strain. All simulations, except that one which relates to cyan, show the same behaviour at lower global strains. The Poisson's effect is the dominant effect and induces the compressive stresses. Transverse plastic flow occurs in every simulation at about 6 % global strain. In principle the compressive stress at the end of the simulation is depended on the yield limit and hardening behaviour in copper. The damage initiation in chrome is not relevant for the transverse stress.

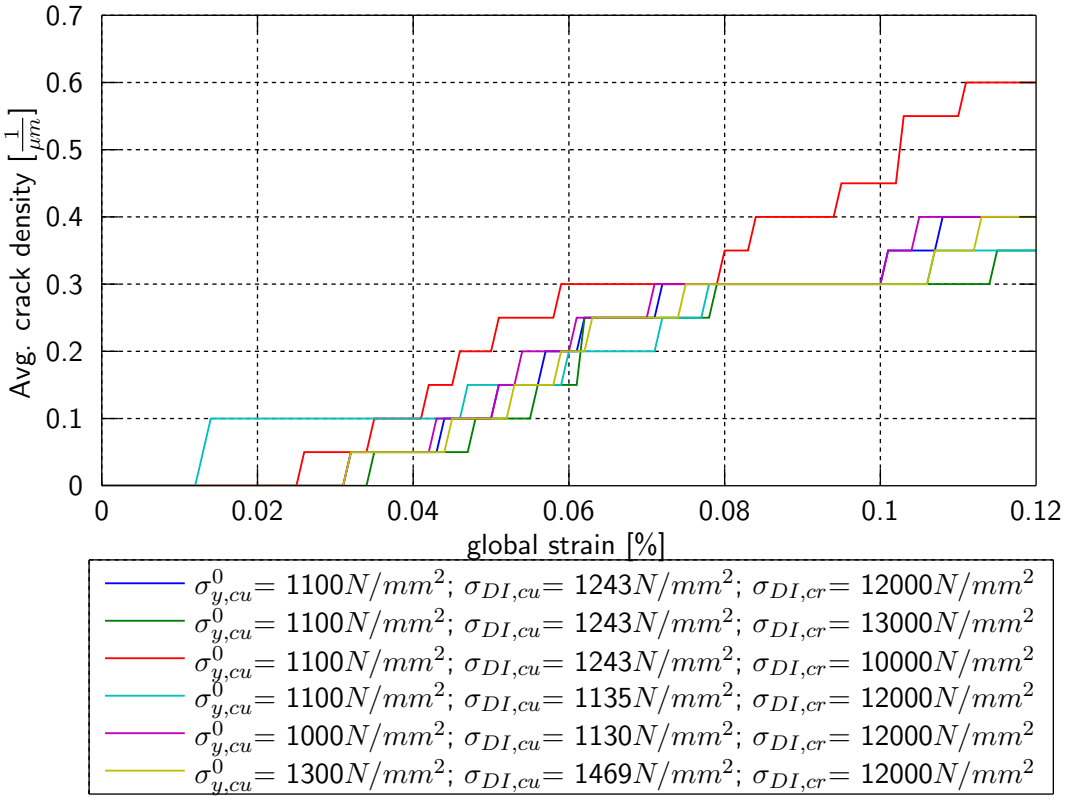

Figure 3.22: Average crack densitys dependent on the global strain from several parameter studies.

Figure 3.22 shows that a lower damage initiation stress in chrome leads to a higher crack density. In the 50 nm model the major goal was to reach the crack density from the experiments. This is the case with a damage initiation of about 12000 MPa. This value is used in further simulations with thicker copper films.

The average crack widths are shown in Fig. 3.23. They are similar and too small (compare with Tab. 3.1). Interesting is the behaviour of the "cyan simulation". Although

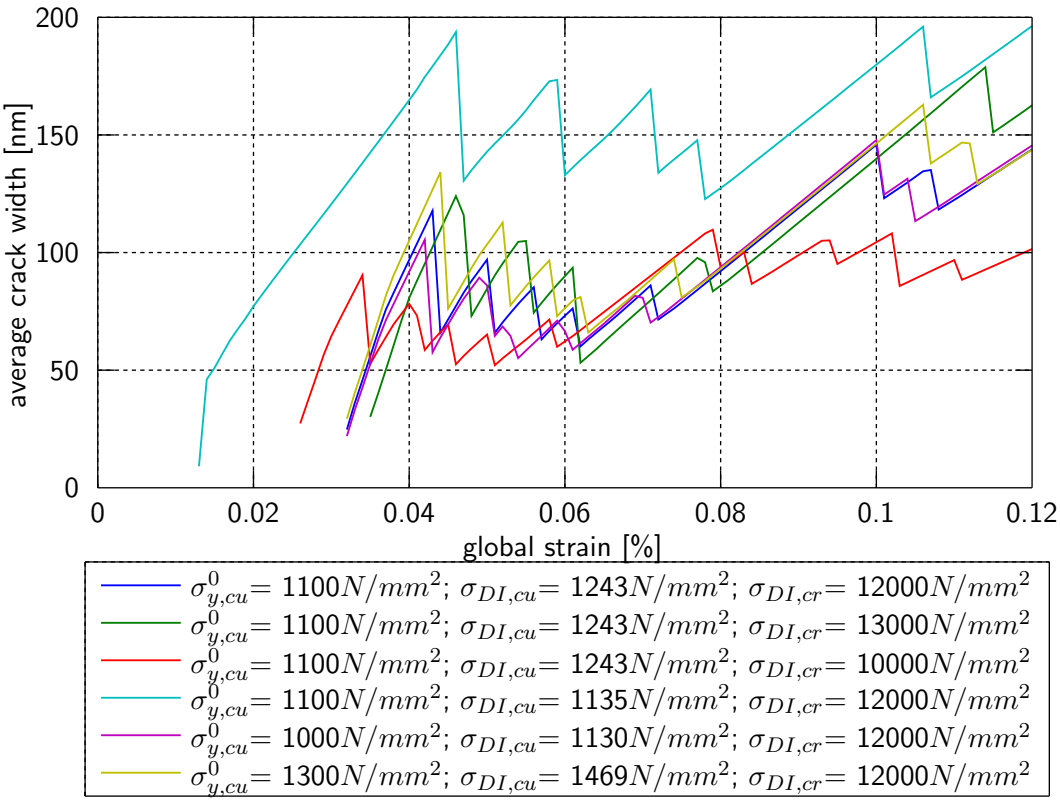

Figure 3.23: Average crack width dependent on the global strain from several parameter studies.

most of the parameters are the same as in the other simulations, the crack width is very high.

Chapter 4

Film system with a 100 nm copper layer

The experiments performed at the MPIE showed some differences between the 50 nm and the 100 nm film. The crack density decreases in copper and remains the same in chrome. The measured longitudinal stress (Fig. 3.13a) at high global strains is lower than the one in the 50 nm copper layer. Here the goals are to explain these measured effects by simulations and to find explanations.

4.1 Material laws in the model

Basically, here were used the same material laws as in Chapter 3.1. Some parameters were adjusted, but the qualitative behaviours of the materials remain the same. As the experiments have shown (Fig. 3.13a), the yield limit of copper in the 100 nm film is probably much lower than in the 50 nm film. Even the hardening parameters could be different. But the focus here is to show the influences of lower yield limits in copper. Therefore, the yield limits 600 MPa, 800 MPa and 1100 MPa are used.

4.2 Definition of the cohesive zones in the model

The parameters of the cohesive zones are equal to that used in the 50 nm film model. The samples out of a normal distribution for the calculation of the damage initiation

stresses in copper and chrome are the same as in the 50 nm model. Reason for that is the comparability of the crack locations in x–direction in different layer thicknesses.

4.3 Results from FE–analyses

4.3.1 New findings shown in a specific simulation

To point out some differences or similarities a simulation with 600 MPa yield limit in copper and a mean damage initiation stress in chrome of 12000 MPa is used. Figure 4.1 shows the 100 nm model after 12 % global strain. The amount of cracks is not really lower than in the 50 nm model. Often they are even at the same positions. The crack procedure is also the same as in the 50 nm model. Every chrome crack leads to a copper crack, and chrome breaks always at first, with one exception. This exception will be explained later.

Figure 4.1: Overall model with the resulting cracks at a global strain of 12 %.

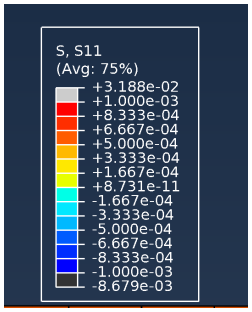

Figure 4.2: Longitudinal stress levels for the following fringeplots. These stress levels are convenient to see effects in the copper layer.

Figure 4.3 shows the crack formation in the 100 nm model and the corresponding stress levels are in Fig. 4.2. The processes are very similar to the ones in the 50 nm model. Therefore, they are not explained again. One difference is that the necking is much more developed. The thicker copper film has no significant influence on the crack propagation.

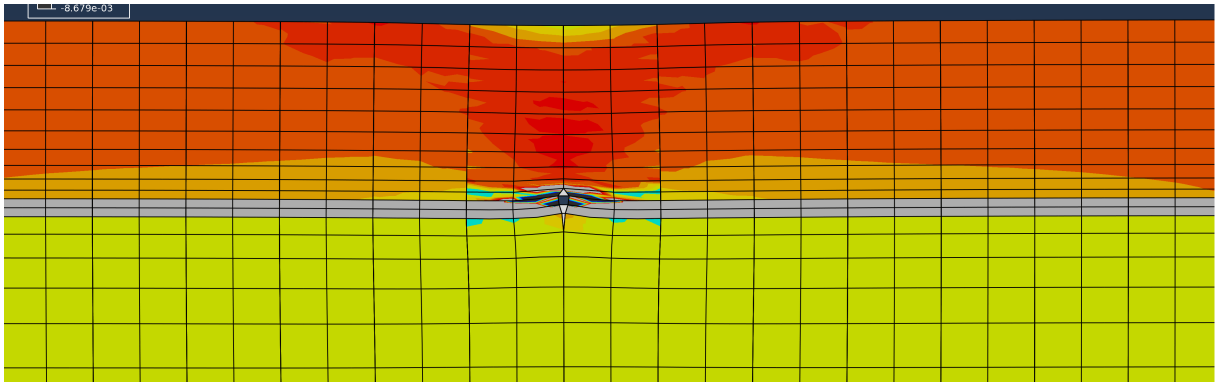

(a) Start of crack formation in copper at a global strain of 3.9787 %.

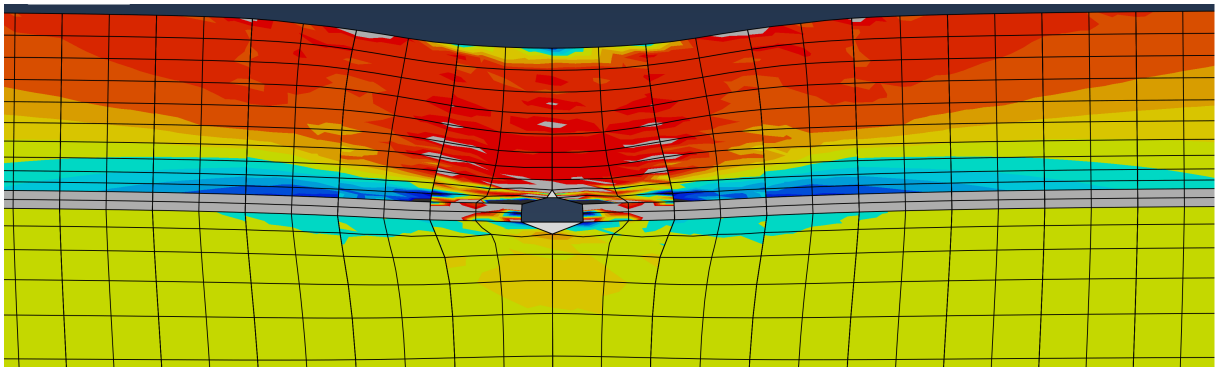

(b) crack propagation through copper at a global strain of 3.9847 %.

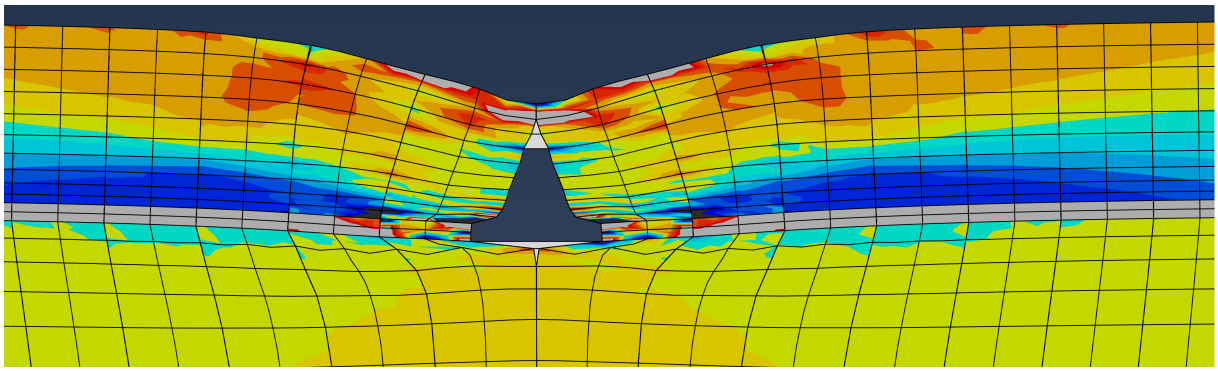

(c) Nearly cracked copper layer at a strain of 4.0003 %.

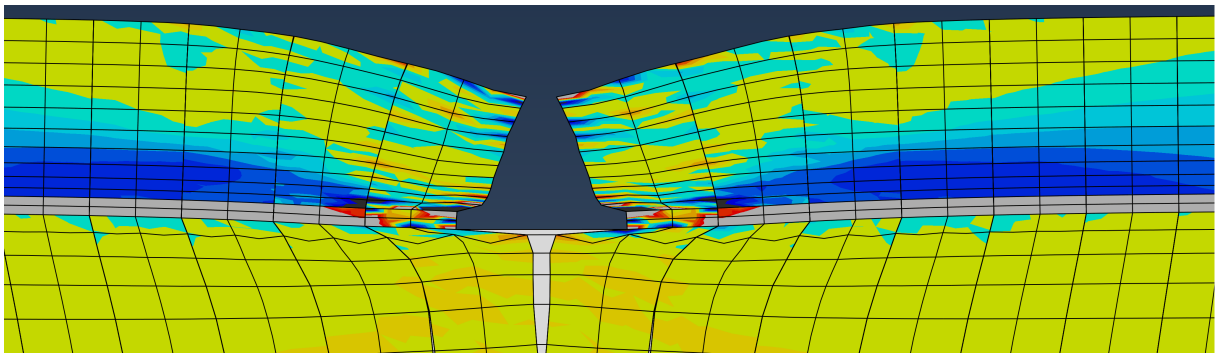

(d) Open crack at a strain of 4.0612 %.

Figure 4.3: Plots of longitudinal stress with limits for the copper layer. In this simulation is the yield limit in copper at 600 MPa.

4.3.2 Summarized results from several parameter studies

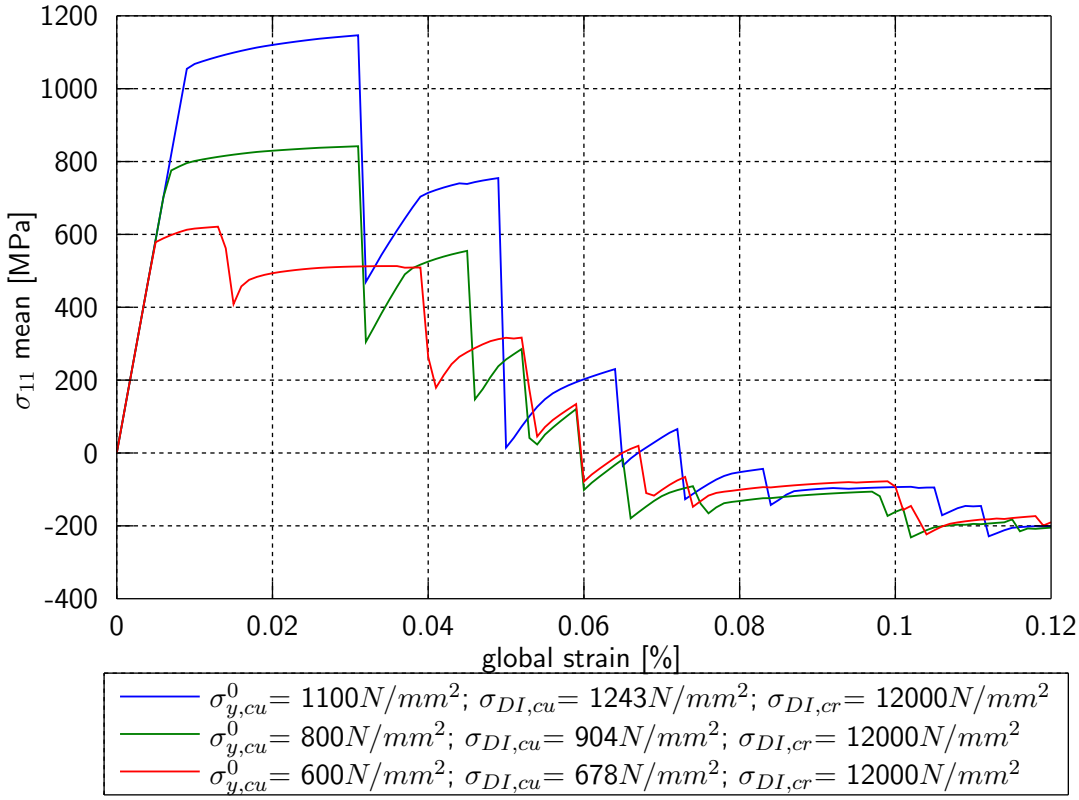

Figure 4.4: Mean stresses in longitudinal direction in copper from several parameter studies.

In Fig. 4.4 the longitudinal mean stress in copper is shown. These parameter studies were made with three different yield limits in copper. All other parameters are equal and the damage initiation strain in every study is approximately 14 %. This figure shows that the yield limit has no major influence on the mean stress level in longitudinal direction at higher global strains. As already mentioned the elastic spring back in chrome leads after the appearance of a crack to a compression of the copper layer. In the 100 nm model chrome has to compress more copper with the same elastic energy. Thus, the mean stress in copper at high global strains is higher than in thinner layers and this effect depends only on the layer thickness and not on material properties. In the "red simulation" one can find a crack at a very low global strain. Due to the statistical distribution of the damage initiation stresses, a very low value appears at this position. This results in a crack, which starts in copper. This is the only simulation in which fracture of copper

occurred before fracture of chrome.

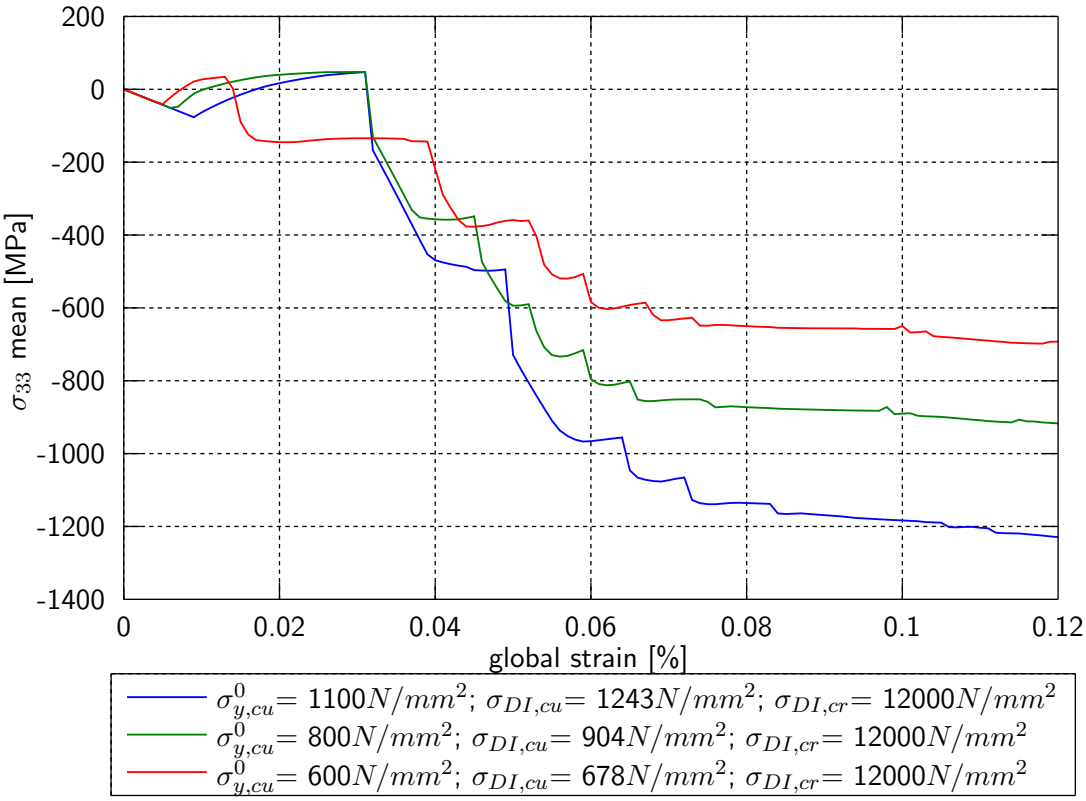

Figure 4.5: Mean stresses in transverse direction in copper from several parameter studies.

The mean transverse stress in copper at high global strains, shown in Fig. 4.5, is strongly dependent on the yield limit. The behaviour is the same as in the 50 nm model. Due to the Poisson's effect very high compressive stresses in transverse direction occur. Again, they do not match with the measurements in Fig. 3.13b.

The crack densities in Fig. 4.6 are almost equal to the ones in the 50 nm model. They are not really dependent on the yield limit and the layer thickness in this model. But the measurements in Fig. 3.15 show a different behaviour. The crack density, especially at higher global strains, is much lower than in the 50 nm layer. From this one can conclude, that other material properties are responsible for the lower crack densities.

The average crack widths in Fig. 4.7 are lower than in the experiments, and the yield limits have no observable influence.

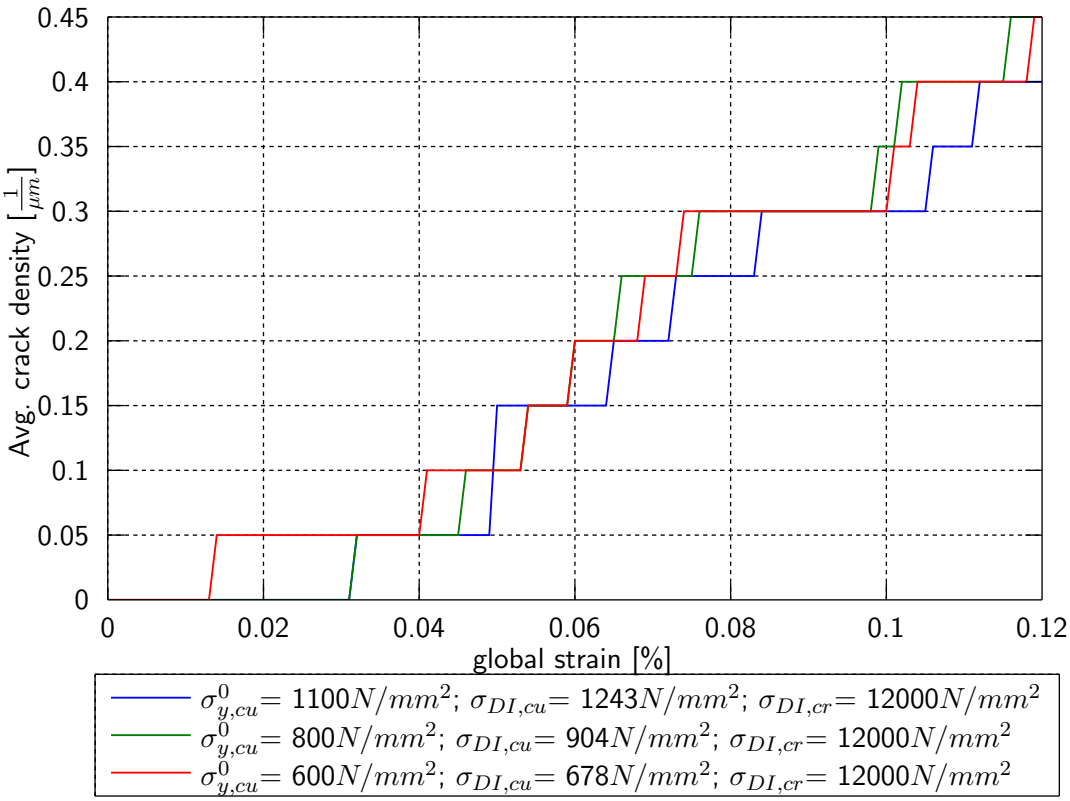

Figure 4.6: Average crack densities dependent on the global strain from several parameter studies.

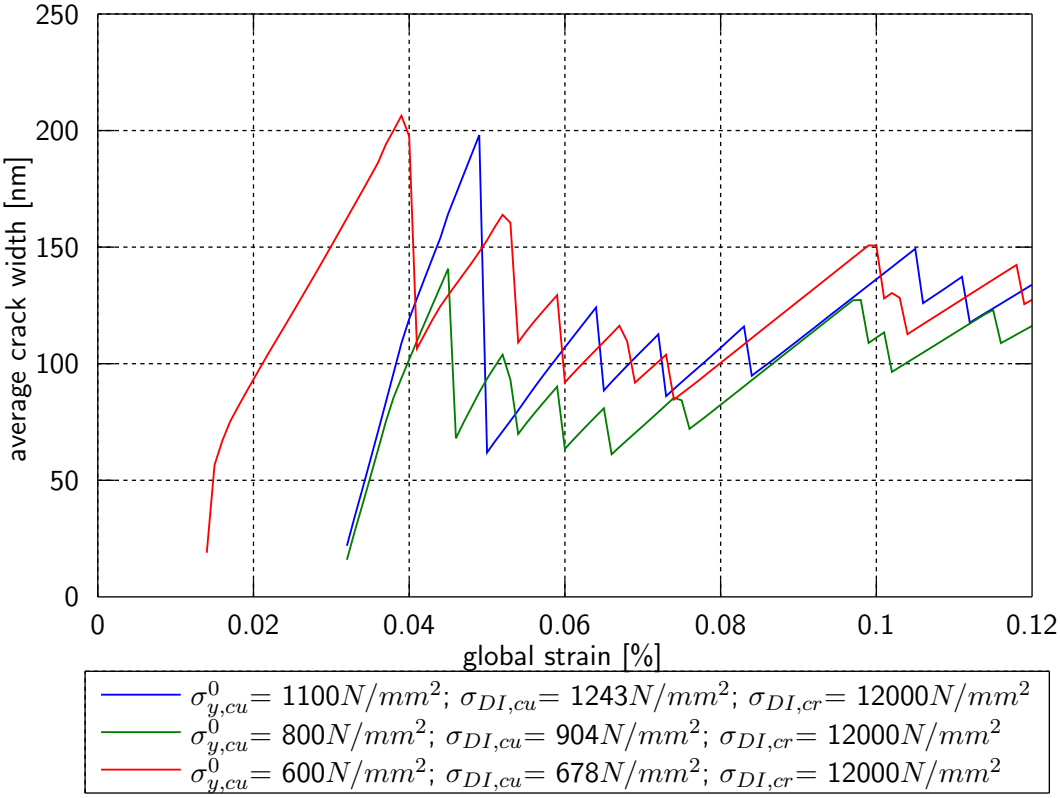

Figure 4.7: Average crack width dependent on the global strain from several parameter studies.

Chapter 5

Film system with a 200 nm copper layer

Experiments showed definitely that there are chrome cracks which do not lead to a copper crack in the samples with 100 and 200 nm thick copper layers (Fig. 5.1). Using the same

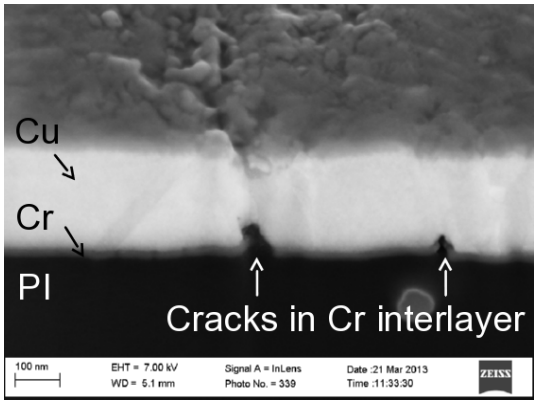

Figure 5.1: FIB cross section through a crack in a flexible film system with a 200 nm thick copper layer. There are detectable chrome cracks which don't lead to a copper crack. (This picture is provided by MPIE.)

material parameters as for the 100 nm models, no copper cracks could be observed without chrome cracks. The amount of cracks was still the same and the cracks were even at the same positions as in the 50 nm model. Also computations with different yield limits in copper did not bring new knowledge. Therefore, the influence of the hardening of the copper layer and the fracture energy of the cohesive zone in copper were investigated. It will be shown, that the hardening and the fracture energy density (energy release rate)

have a significant influence on the computed results.

5.1 Material laws in the model

Here stress–strain behaviours with stronger hardening are used because the measurements of longitudinal stresses showed hardening in the thicker copper layers in the first 3 % of global straining (Fig. 1.4a). Again the hardening is assumed to be linear, but the slope of the stress–strain curve after the yield limit is much higher. In Fig. 5.2 two possibilities are pictured. These two stress–strain curves are used in the simulations, their results are summarized in Chapter 5.3.

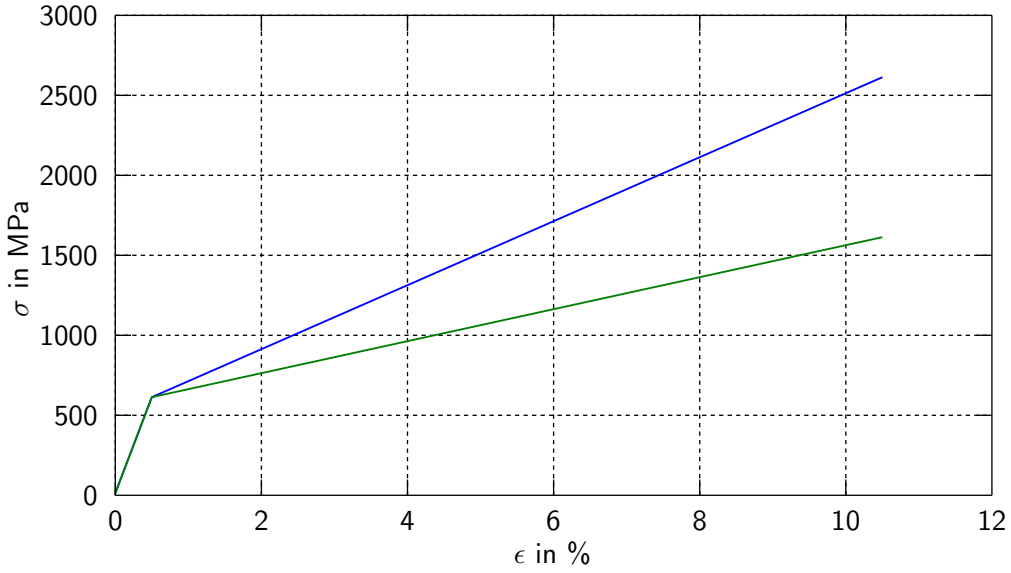

Figure 5.2: Two possibilities of a stress–strain curve in copper

In one simulation the mean damage initiation stress in chrome is changed from 12000 MPa to 6000 MPa (but this will be pointed out again). The material parameters in polyimide are equal to those used previously.

5.2 Definition of the cohesive zones in the model

The cohesive zones in chrome and polyimide are unchanged. Chrome is still brittle. The fracture energy in polyimide is infinite anyway.

5.2.1 Cohesive zones in copper

The traction separation law was already explained in Chapter 2.1 and Chapter 3.2.1. There was a rather brittle material behaviour with a separation of complete failure δ_n^f of 0.6 nm assumed. Now a ductile material behaviour is assumed in some simulations. So δ_n^f in the cohesive zone is now 10 nm instead of 0.6 nm. This value is realistic for a ductile material when one compares δ_n^f with the proportions of the model. Lower and higher fracture energy densities produced poor results.

5.3 Results from FE–analyses

5.3.1 New findings shown in a specific simulation

To show the influences of fracture energy, hardening behaviour and mean damage initiation stresses in chrome and copper, the in Tab. 5.1 listed parameters are used for the following simulation.

Parameter	Parametervalue
fracture energy density	$\delta_n^f = 10\,nm$ (ductile)
hardening modulus	$E_{hard} = 10000\,MPa$
yield limit copper	$\sigma_y^0 = 600\,MPa$
ultimate stress copper	$\sigma_{u,cu} = 1600\,MPa$
Ultimate stress chrome	$\sigma_{u,cr} = 6000\,MPa$

Table 5.1: Parameters for the following FE-simulation.

Figure 5.3: Overall model with the resulting cracks at a global strain of 12 %.

Figure 5.3 shows five copper cracks in this simulation. But there are a lot more chrome cracks. Unfortunately, they are not recognisable in this figure. It seems, that the higher fracture energy attenuates the stress concentration due to chrome cracks. The lower damage initiation stress in chrome is responsible for much more cracks in chrome.

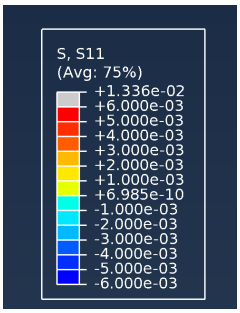

Figure 5.4: Longitudinal stress levels for the following fringeplots.

There are 63 of them, which are maybe to many. But this shows the influence of a higher fracture energy density very well.

Figure 5.5 shows one of the chrome cracks in Fig. 5.3 (corresponding limits in Fig. 5.4). The chrome breaks and the growing distance between the two chrome sides leads to stress concentrations in copper in the area of the crack tip. Due to the more ductile behaviour of the copper layer, this stress concentration does not lead to fracture of the copper.

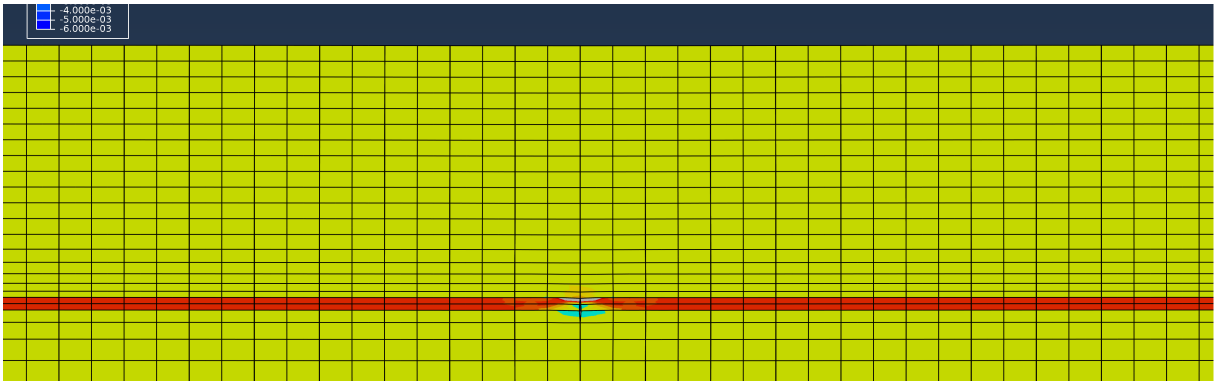

(a) Start of crack formation in chrome at a global strain of 1.6136 %.

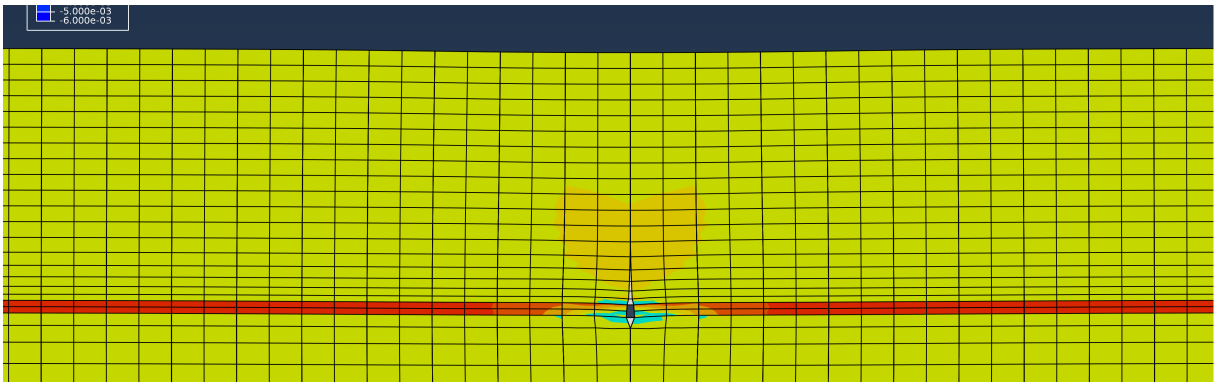

(b) End of crack formation in chrome at a global strain of 1.8497 %.

Figure 5.5: Plots of longitudinal stress and a chrome crack which do not result in a copper crack.

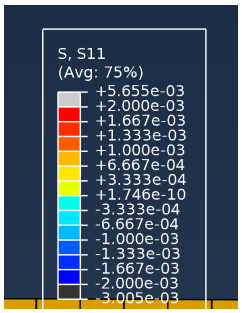

Figure 5.6: Longitudinal stress levels for the following fringeplots.

Figure 5.8 shows the crack formation in copper (corresponding limits in Fig. 5.6). In Fig. 5.8a and Fig. 5.8b the area of stress concentration is obvious. The crack grows from chrome to the surface and leads there to necking due to high plastic strains. It's obvious, that the compressive stress in copper is much lower than in the previous simulations. The reason for this is the lower damage initiation stress in chrome but also the thicker copper layer, as already mentioned before.

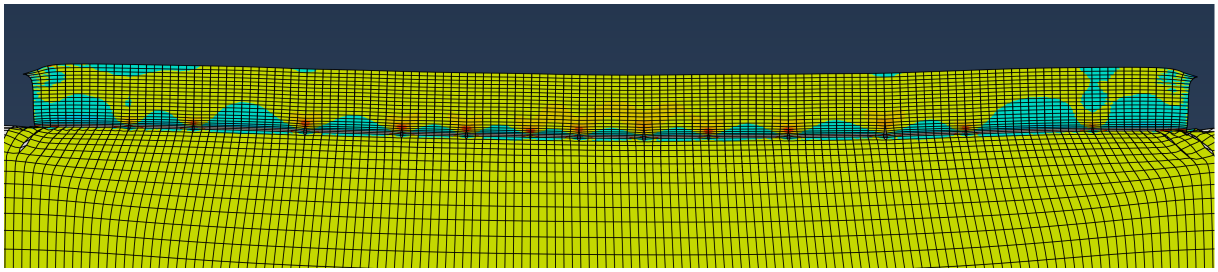

Figure 5.7: Plots of longitudinal stress and chrome cracks between two copper cracks at positions of stress concentration at a global strain of 12 %.

The red areas in Fig. 5.7 show the chrome cracks between two copper cracks. The crack density grows with the distance to the copper crack. Reason for that is the unloading of the chrome layer due to fracture of copper. Here is the tensile stress state in copper clearly visible.

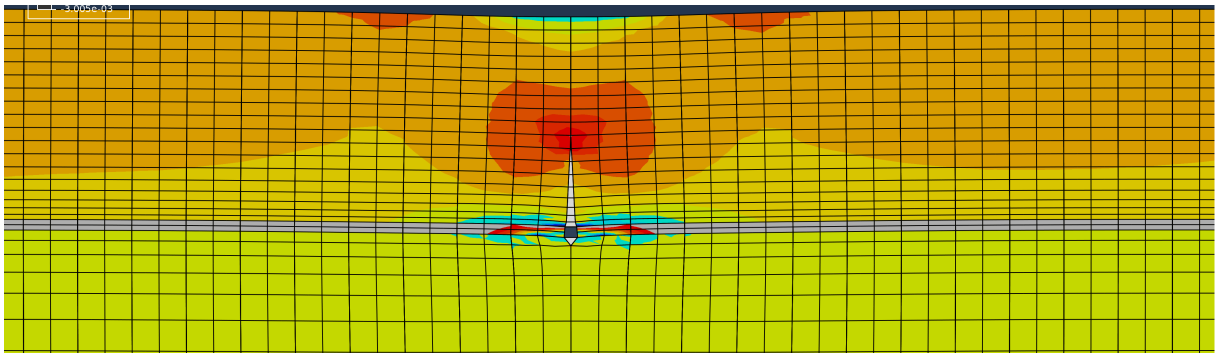

(a) Start of crack formation in copper at a global strain of 1.9625 %.

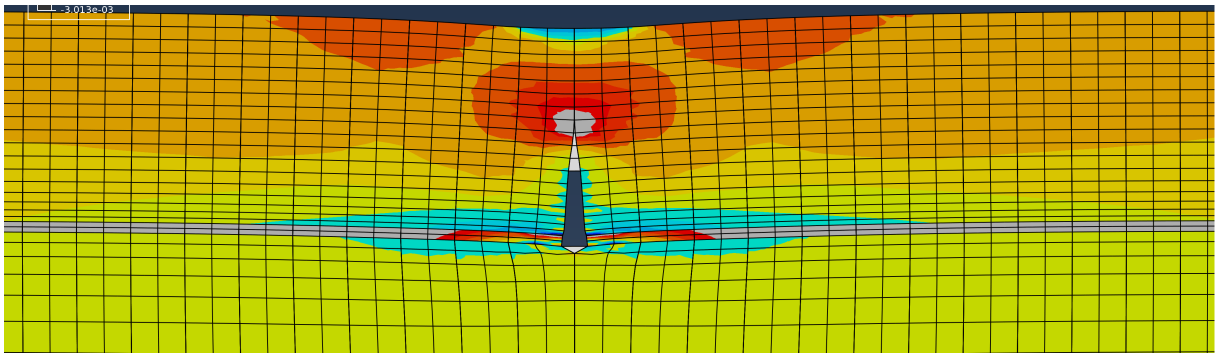

(b) Crack formation in copper at a global strain of 1.9764 %.

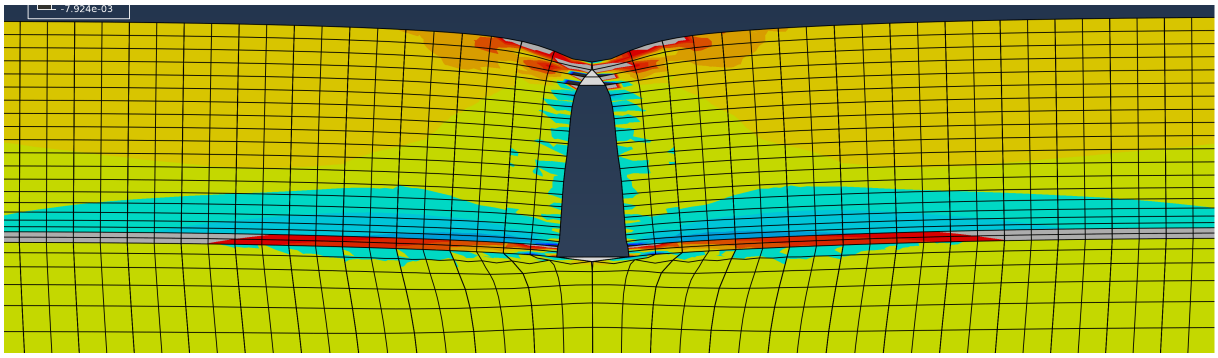

(c) Crack formation in copper at a global strain of 2.0125 %.

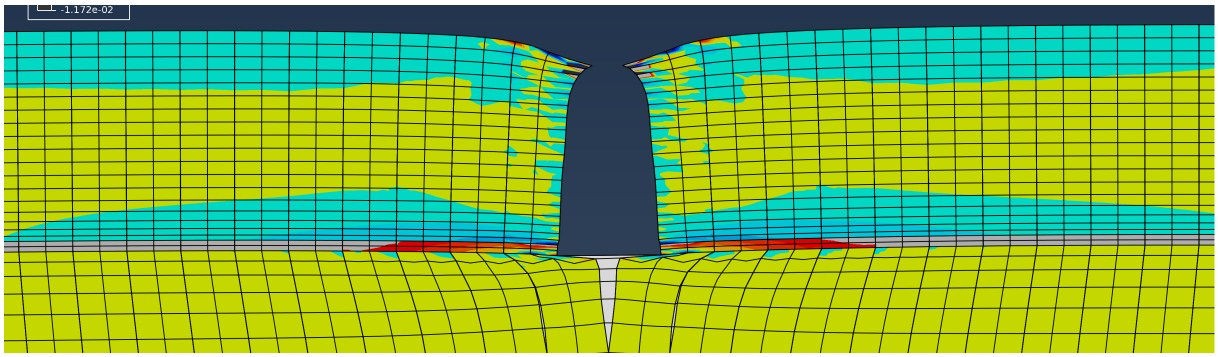

(d) Broken through copper at a global strain of 2.0932 %.

Figure 5.8: Crack formation and longitudinal stress in copper.

5.3.2 Summarized results from several parameter studies

In this section six different simulations are compared. The first three of them (blue, green and red) were computed with the same parameters as the simulations in Chapter 4. In these three simulations the copper is modelled rather brittle and with weak hardening. In the other three simulations the copper is modelled rather ductile with a separation of complete failure δ_n^f of 10 nm. Also the hardening behaviour of copper is much more distinct. The golden curve in the following four figures is the example simulation in Chapter 5.3.1.

Figure 5.9 shows the mean longitudinal stress in copper. Compared with simulations performed for other layer thicknesses the stress levels at high global strains are slightly higher, especially in the "cyan" and "gold" simulations they are even positive.

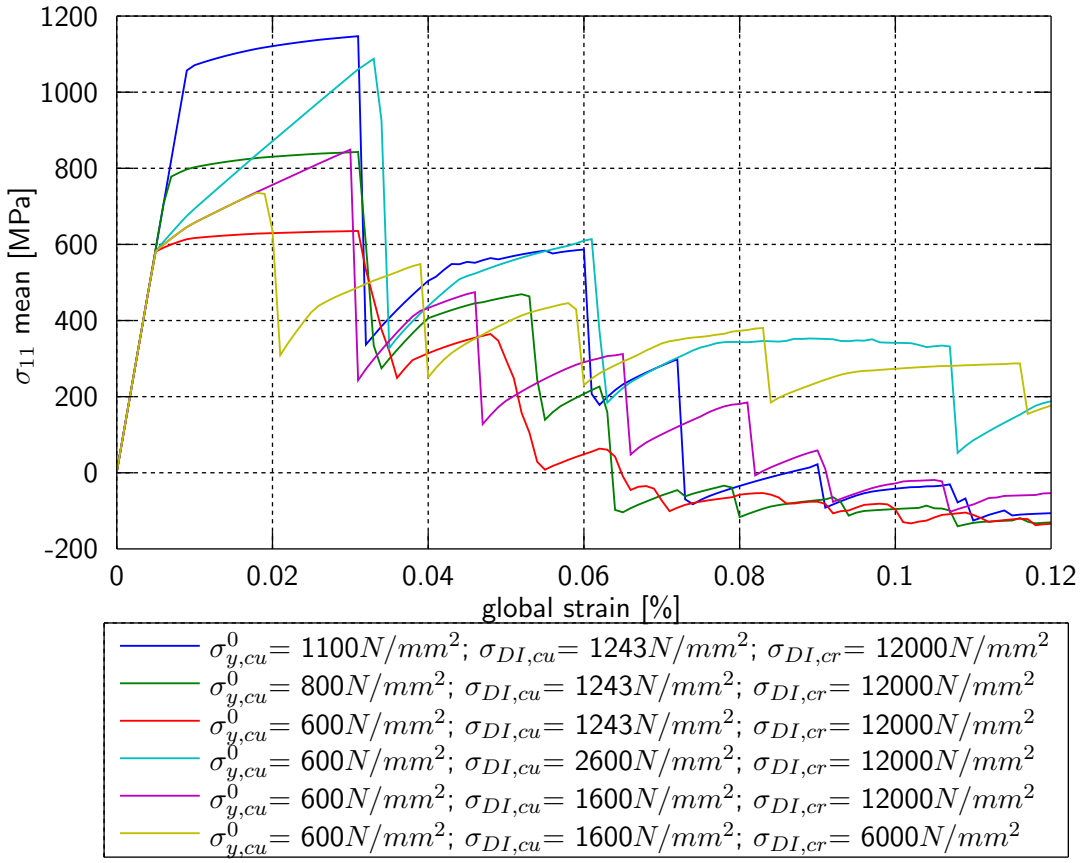

Figure 5.9: Mean stresses in longitudinal direction in copper from several parameter studies.

In Fig. 5.10 no new information can be found. All effects and behaviours were pointed out already before.

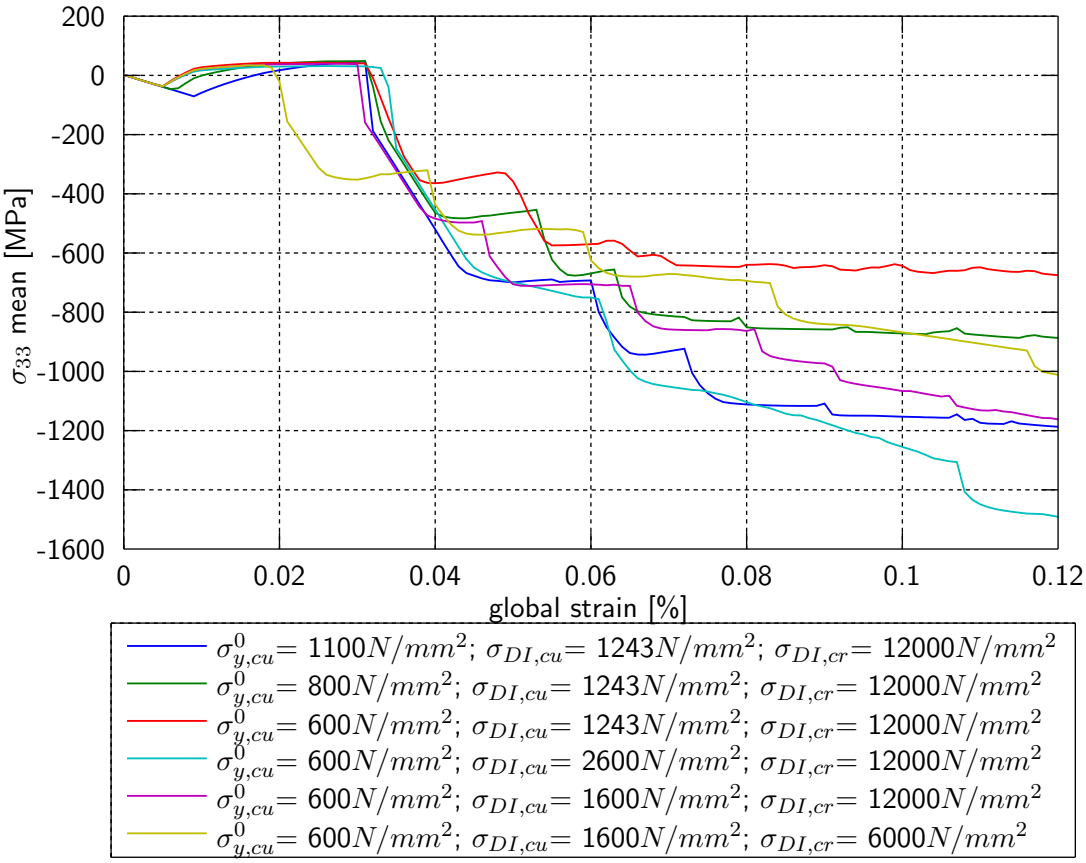

Figure 5.10: Mean stresses in transverse direction in copper from several parameter studies.

The average crack densities in Fig. 5.11 are interesting. In the "cyan" and "gold" simulation the crack density is not far away from the ones in the experiments, but there's no indication of a saturation which is reached in the experiments. Due to the fact, that a formation of chrome cracks without building a copper crack is possible, the crack density in copper decreases and is not as dependent on the damage initiation stress in chrome as before. The crack density in the "magenta" simulation is even higher than in the "golden".

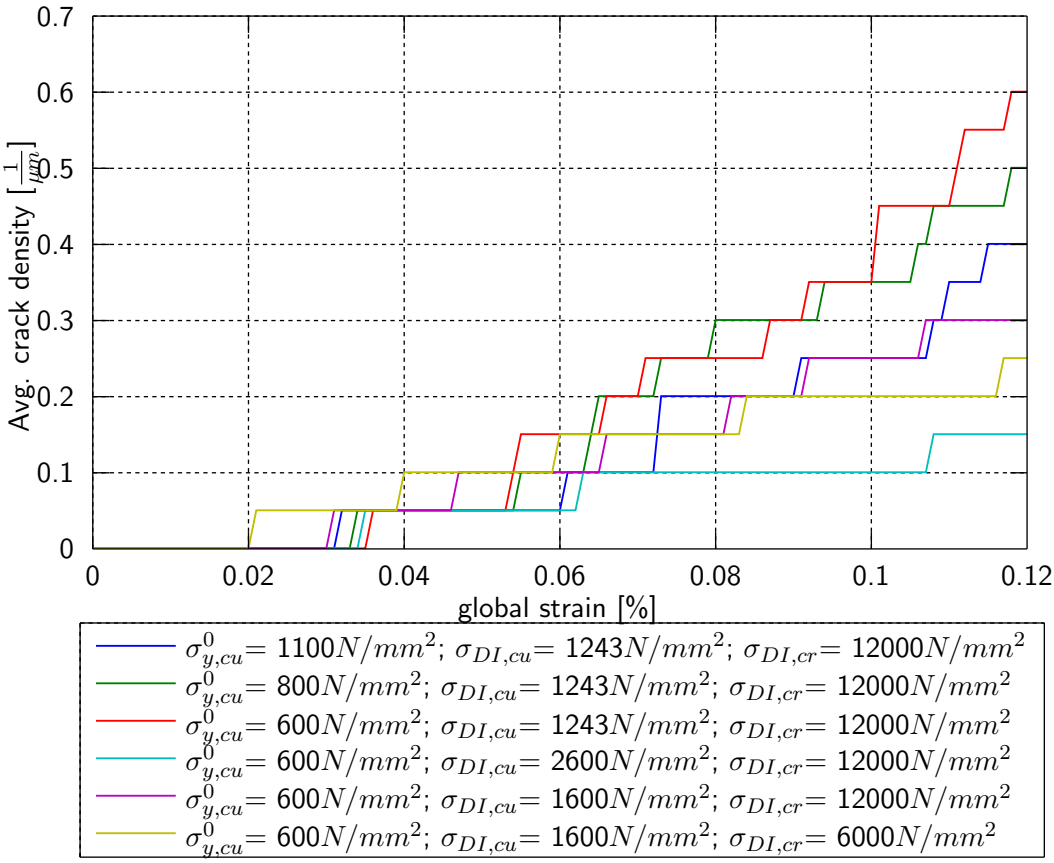

Figure 5.11: Average crack densitys dependent on the global strain from several parameter studies.

average crack width [nm]	distance between cracks [μm]	global strain [%]
551 +/- 138	7.38 +/- 3.92	5
573 +/- 160	7.12 +/- 4.9	12
520 +/- 128	5.55 +/- 3.63	15

Table 5.2: Measurements of average crack widths and distances between cracks for the 200 nm copper layer.

The average crack widths Fig. 5.12 are still too low compared with measurements (Tab. 5.2). This might have an influence on all stresses in copper and also on the crack density, because a higher crack width reduces the effective local strain in the film segments between the cracks as mentioned in Chapter 3.

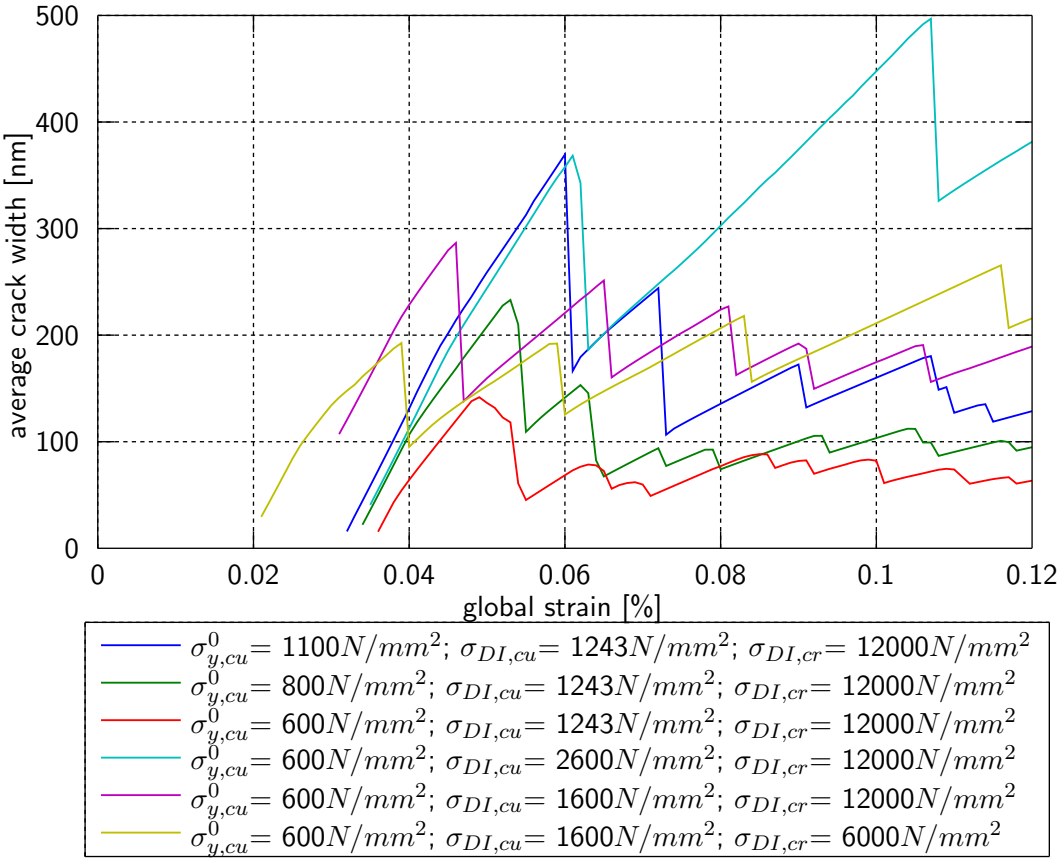

Figure 5.12: Average crack widths dependent on the global strain from several parameter studies.

Chapter 6

Statistical evaluation of the film stresses in copper

In Chapter 1 the in–situ stress measurement with synchrotron X–ray diffraction was mentioned. This method calculates stress values based on the measurement of distances between lattice planes in a volume under a measuring area of a view μm^2. So one obtains a lot of stress values out of the measured region. In a nearly homogeneous stress state the range of the stress values would be narrow. But in this research work the measuring area includes cracks and necks and stress values in a large range appear. Therefore, it is important to make statistical distributions and to build mean stress values from calculated values in the measured volume. The stress values in Fig. 1.4 were calculated as the mean value corresponding to a normal distribution of the measured values. But it is not clear, if a normal distribution is representative for the distribution of the stress values in the copper film. For this purpose statistical evaluations of the computed film stresses in the three different models were made.

Figure 6.1 shows the distribution of the film stresses from the model with the 50 nm thick copper layer in Chapter 3 at five different global strains. The stress ranges in the histograms are 200 MPa and the vertical axis shows the fraction of the entire copper layer. The global strain of the first crack is approximately 3 % and therefore the first figure shows already a broken structure. The peak in Fig. 6.1a is higher than 0.5, but for reason of clarity all figures have the same axis limits. The figures show that the distribution changes

the shape. This could have an influence on building of mean stress values. As mentioned in Chapter 3 the film stresses from initial tensile stresses shift to compressive stresses at high global strains.

With these histograms propositions can be made if a bending stress state occurs. A pure bending stress state would have the shape of a rectangle in a histogram. Some of the histograms show kind of such behaviour. Maybe a bending stress state has an influence on the building of mean stress values.

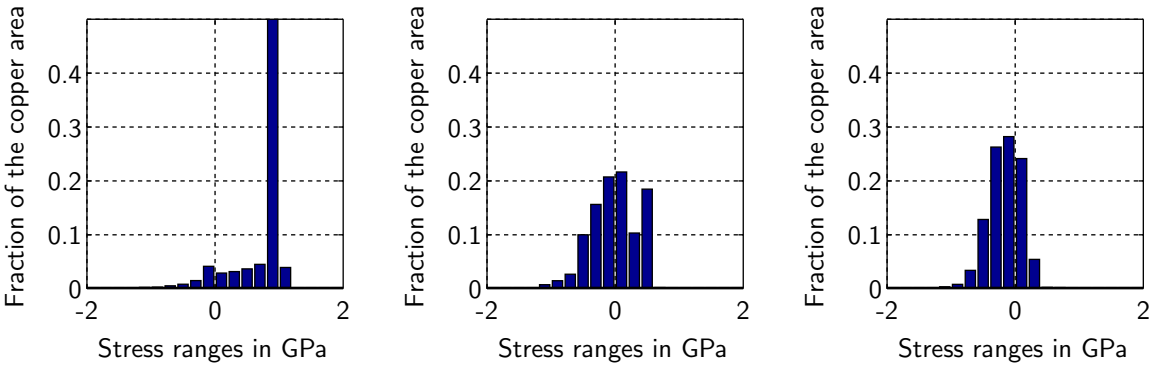

(a) Stress distribution at 4 % global strain (b) Stress distribution at 6 % global strain (c) Stress distribution at 8 % global strain

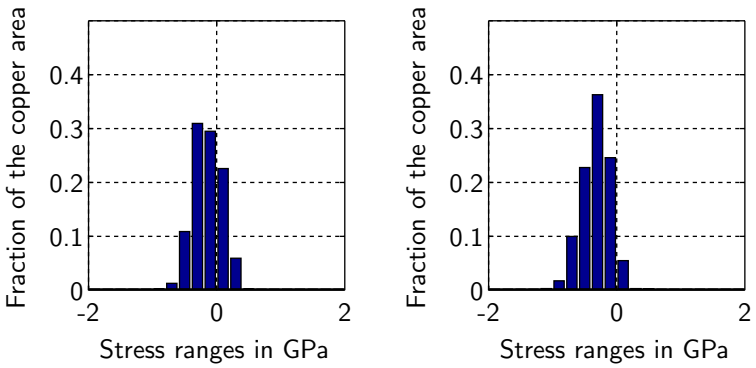

(d) Stress distribution at 10 % global strain (e) Stress distribution at 12 % global strain

Figure 6.1: Stress distribution at different global strains in the film system with a 50 nm copper layer.

Figure 6.2 shows the distribution of film stresses from the model in Chapter 4. The histograms show similar behaviours as in the previous.

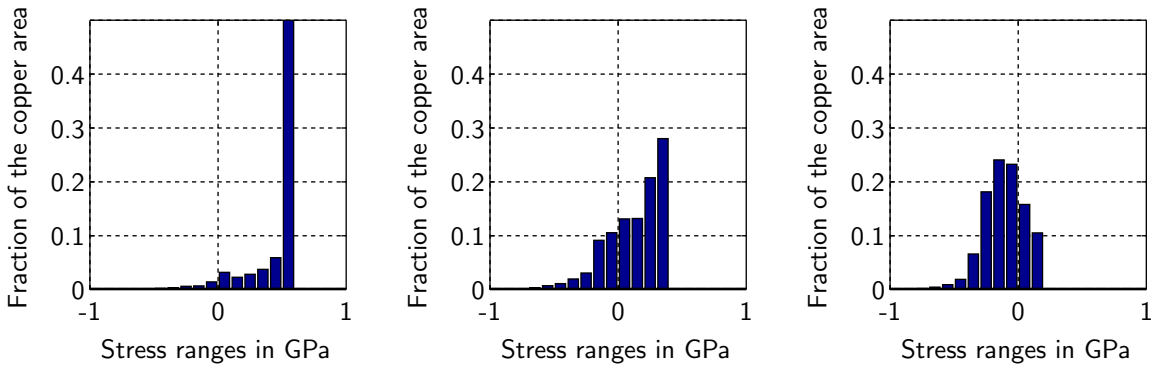

(a) Stress distribution at 4 % global strain (b) Stress distribution at 6 % global strain (c) Stress distribution at 8 % global strain

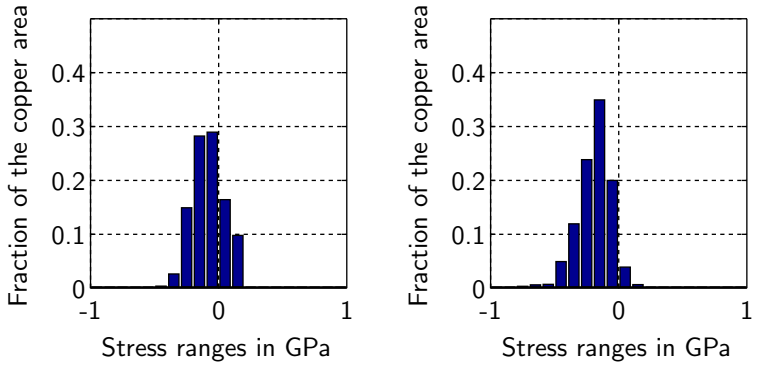

(d) Stress distribution at 10 % global strain (e) Stress distribution at 12 % global strain

Figure 6.2: Stress distribution at different global strains in the film system with a 100 nm copper layer.

Figure 6.3 shows the distribution of film stresses from the model in Chapter 5. The range of the film stresses is wider than in distributions of previous models and tensile stresses are dominant.

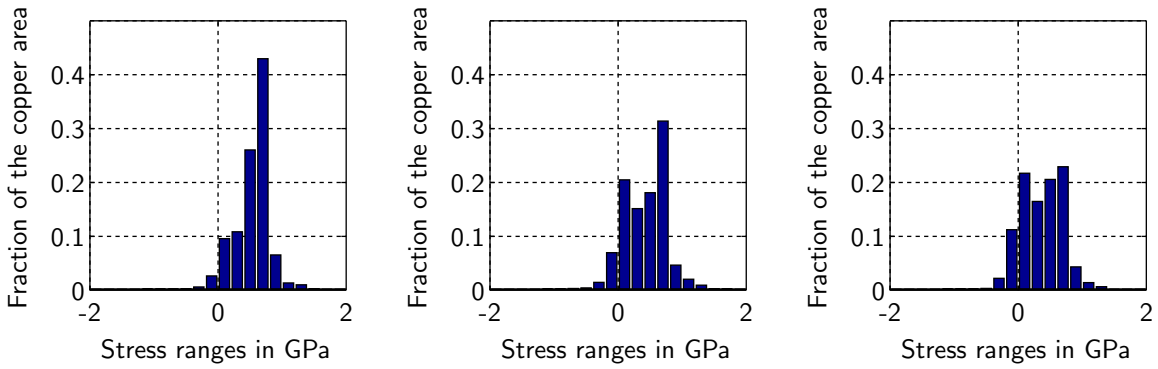

(a) Stress distribution at 4 % global strain (b) Stress distribution at 6 % global strain (c) Stress distribution at 8 % global strain

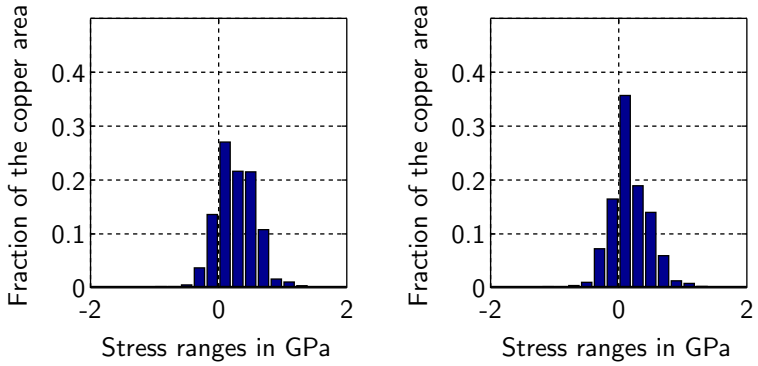

(d) Stress distribution at 10 % global strain (e) Stress distribution at 12 % global strain

Figure 6.3: Stress distribution at different global strains in the film system with a 200 nm copper layer.

Chapter 7

Conclusion

Because of the high dependency of the behaviour on material parameters, which are not directly measurable, a realistic modelling of flexible film systems is not easy. Unfortunately, the determination of material parameters and behaviours of such thin films is still a problem in material science. In addition there is a geometric influence on the material properties, this is because the layer thickness has an influence on the morphology and on the mechanisms of plastic deformations. In a flexible film system every layer has an influence on the other layers and it is not possible to investigate every material layer separately. To get an idea about the dependence of the models on the material parameters, parameter studies were carried out. These parameter studies are numerically very expensive. The calculation time of one study amounts approximately to 10 hours. This also includes the evaluation of mean stresses and crack densities. Nevertheless, some trends could be pointed out.

In all models the formation of cracks always starts in chrome. The reason for this is a lower ultimate strain in the pure elastic chrome than in the elastic–plastic copper. The crack density in chrome depends on its ultimate stress and ultimate strain, respectively. The ultimate stress in such thin chrome films can be very high. Assuming a ultimate stress of 12000 MPa the obtained simulation results for the crack densities match well with the experiments.

If the copper is assumed as being brittle every crack in chrome leads to fracture of the overlaying copper layer independent from the layer thickness. This is due to the stress concentration introduced by the crack in chrome. Only the fracture energy density in copper can attenuate the stress concentration in a way so that not every chrome crack leads to a copper crack. The determination of fracture energy densities is not easy. Assuming a ductile material behaviour in copper makes it possible to obtain crack densities similar to the experimentally observed ones. Therefore, the crack density in copper is strongly dependent on the fracture energy density in copper.

The mean stresses in transverse direction obtained through simulations are not comparable with those determined in the experiments. There are no similarities, not even in the linear elastic parts of the loading history. At the present point no explanation for this difference can be given.

The level of longitudinal mean stress at high global strains is strongly dependent on the layer thickness of copper and the crack density in copper. At the moment the copper breaks, the purely elastic chrome springs back releasing most of its strain energy. Since chrome has the same layer thickness in all considered configurations, the elastic energy released during spring back is always nearly the same. The spring back reduces the longitudinal tensile stress in the copper layer until equilibrium is reached. In the 50 nm model this effect always leads to compressive stresses because copper was deformed plastically prior to cracking. It would need more energy to reach the same stress state in a thicker copper layer. Therefore, the longitudinal mean stress remains higher for thicker copper layers.

List of Figures

List of Tables

Bibliography

[1] *Abaqus Analysis Users's Guide Version 6.13.*

[2] *Abaqus Theory Guide Version 6.13.*

[3] *Altair Hyper Works Version 12.0 Desktop User Guide.*

[4] Megan J. Cordill. Flexible film systems: Current understanding and future prospects. *JOM*, 62(6):9–14, 2010.

[5] Lothar Spiess, Gerd Teichert, Robert Schwarzer, Herfried Behnken, Christoph Genzel. *Moderne Röntgenbeugung: Röntgendiffraktometrie für Materialwissenschaftler, Pysiker und Chemiker.* Vieweg + Teubner Verlag, 2009.

[6] Teng Li, Zhenyu Huang, Z. Suo, Stéphanie P. Lacour, and Sigurd Wagner. Stretchability of thin metal films on elastomer substrates. *Applied Physics Letters*, 85(16):3435–3437, 2004.

[7] F. Toth, F. G. Rammerstorfer, M. J. Cordill, and F. D. Fischer. Detailed modelling of delamination buckling of thin films under global tension. *Acta Materialia*, 61(7):2425 – 2433, 2013.

[8] Khaled M. Youssef, Ronald O. Scattergood, K. Linga Murty, Joseph A. Horton, and Carl. C. Koch. Ultrahigh strength and high ductility of bulk nanocrystalline copper. *Applied Physics Letters*, 87(9):–, 2005.